The Onset of Thermally Unstable Cooling from the Hot Atmospheres of Giant Galaxies in Clusters: Constraints on Feedback Models

M. T. Hogan[1,2], B. R. McNamara[1,2] , F. A. Pulido[1] , P. E. J. Nulsen[3,4] , A. N. Vantyghem[1] , H. R. Russell[5], A. C. Edge[6] ,
Iu. Babyk[1,7] , R. A. Main[8], and M. McDonald[9]

[1] Department of Physics and Astronomy, University of Waterloo, Waterloo, ON, N2L 3G1, Canada; m4hogan@uwaterloo.ca
[2] Perimeter Institute for Theoretical Physics, Waterloo, ON, N2L 2Y5, Canada
[3] Harvard-Smithsonian Center for Astrophysics, 60 Garden Street, Cambridge, MA 02138, USA
[4] ICRAR, University of Western Australia, 35 Stirling Highway, Crawley, WA 6009, Australia
[5] Institute of Astronomy, Madingley Road, Cambridge, CB3 0HA, UK
[6] Centre for Extragalactic Astronomy, Department of Physics, Durham University, Durham, DH1 3LE, UK
[7] Main Astronomical Observatory of NAS of Ukraine, 27 Academica Zabolotnogo Str, 03143, Kyiv, Ukraine
[8] Canadian Institute for Theoretical Astrophysics, University of Toronto, 60 St. George Street, Toronto, ON, M5S 3H8, Canada
[9] Kavli Institute for Astrophysics and Space Research, Massachusetts Institute of Technology, 77 Massachusetts Avenue, Cambridge, MA 02139, USA
Received 2017 March 29; revised 2017 September 18; accepted 2017 November 2; published 2017 December 13

Abstract

We present accurate mass and thermodynamic profiles for 57 galaxy clusters observed with the *Chandra X-ray Observatory*. We investigate the effects of local gravitational acceleration in central cluster galaxies, and explore the role of the local free-fall time (t_{ff}) in thermally unstable cooling. We find that the radially averaged cooling time (t_{cool}) is as effective an indicator of cold gas, traced through its nebular emission, as the ratio t_{cool}/t_{ff}. Therefore, t_{cool} primarily governs the onset of thermally unstable cooling in hot atmospheres. The location of the minimum t_{cool}/t_{ff}, a thermodynamic parameter that many simulations suggest is key in driving thermal instability, is unresolved in most systems. Consequently, selection effects bias the value and reduce the observed range in measured t_{cool}/t_{ff} minima. The entropy profiles of cool-core clusters are characterized by broken power laws down to our resolution limit, with no indication of isentropic cores. We show, for the first time, that mass isothermality and the $K \propto r^{2/3}$ entropy profile slope imply a floor in t_{cool}/t_{ff} profiles within central galaxies. No significant departures of t_{cool}/t_{ff} below 10 are found. This is inconsistent with models that assume thermally unstable cooling ensues from linear perturbations at or near this threshold. We find that the inner cooling times of cluster atmospheres are resilient to active galactic nucleus (AGN)-driven change, suggesting gentle coupling between radio jets and atmospheric gas. Our analysis is consistent with models in which nonlinear perturbations, perhaps seeded by AGN-driven uplift of partially cooled material, lead to cold gas condensation.

Key words: galaxies: active – galaxies: clusters: general – galaxies: clusters: intracluster medium – galaxies: elliptical and lenticular, cD – galaxies: kinematics and dynamics – X-rays: galaxies: clusters

1. Introduction

The hot atmospheres at the centers of many galaxies and galaxy clusters radiate X-rays so prodigiously they are expected to cool on timescales much shorter than their ages. Unless radiation losses are compensated by heating, their central atmospheres would cool at rates of hundreds to thousands of solar masses per year and form stars (for a review see Fabian 1994). Observations have instead shown far less molecular gas (Edge 2001; Salomé & Combes 2003), star formation (Johnstone et al. 1987; O'Dea et al. 2008; Rafferty et al. 2008), and cooling gas (Peterson et al. 2003; Borgani et al. 2006; Nagai et al. 2007; Sanders & Fabian 2011) than expected. Cooling must therefore be suppressed. Observation has shown that mechanical feedback from the active galactic nucleus (AGN) within the centrally located brightest cluster galaxy (BCG) to be the most likely mechanism (McNamara & Nulsen 2007).

In the standard picture of AGN feedback, radio jets launched by supermassive black holes (SMBHs) inflate cavities that rise buoyantly through hot atmospheres driving turbulence, shocks, and sound waves (Fabian et al. 2005; Voit & Donahue 2005; Randall et al. 2011; Nulsen & McNamara 2013; Zhuravleva et al. 2014; Hillel & Soker 2016, 2017; Soker 2016; Yang & Reynolds 2016). The enthalpy released by the AGN raises the entropy of the surrounding atmosphere and regulates the rate of cooling (for reviews see McNamara & Nulsen 2007, 2012; Fabian 2012).

Cooling into molecular clouds must occur in order to maintain the feedback cycle. Molecular gas (Edge 2001; Salomé & Combes 2003), nebular emission (e.g., Heckman et al. 1989; Crawford et al. 1999; McDonald et al. 2010; Tremblay et al. 2015), and star formation are indeed observed at levels consistent with having been fueled by cooling from the surrounding hot atmosphere (McNamara et al. 2014; Russell et al. 2017). Feedback is apparently persistent. Cool-core clusters have existed for at least half the age of the universe (e.g., Santos et al. 2010; Ma et al. 2011; Samuele et al. 2011; McDonald et al. 2013; Hlavacek-Larrondo et al. 2015; Main et al. 2017). Their prevalance requires long-term equilibrium between heating and cooling (e.g., Hlavacek-Larrondo et al. 2012; Main et al. 2017), despite large variations of power output from their AGNs (Hogan et al. 2015a).

Nebular emission, increased star formation, and AGN activity are preferentially observed in cluster cores when the central entropy K drops below 30 keV cm^2, roughly equivalent to a central cooling time less than 1 Gyr (Cavagnolo et al. 2008; Rafferty et al. 2008; Sanderson et al. 2009; Main et al. 2017). Though this threshold is sharp, in our view a convincing physical understanding of cooling instability at the

centers of giant galaxies remains elusive. This threshold accurately presages molecular gas in central galaxies at levels far above those seen in normal ellipticals (F. A. Pulido et al. 2017, in preparation, henceforth Paper II), and this molecular gas is likely fueling the AGN feedback cycle (Tremblay et al. 2016). Simulations indicate that inelastic collisions within the Bondi radius may remove angular momentum leading to an inflow of cold gas (e.g., Gaspari et al. 2013). While our understanding of AGN heating has matured, our understanding of thermally unstable cooling is more primitive, but it is a crucial aspect of the feedback cycle.

1.1. Review of t_{cool}/t_{ff} Models and Observations

Hot atmospheres are thought to become thermally unstable in their central regions when the ratio of the cooling time, t_{cool}, to the free-fall time, t_{ff}, of a parcel of cooling gas falls below unity (Cowie et al. 1980; Nulsen 1986). Interest in this problem was revived recently in important papers showing that the instability criterion $t_{cool}/t_{ff} \lesssim 1$ applies to gas cooling in a simulated plane-parallel atmosphere, but may rise well above unity in a three-dimensional atmosphere (McCourt et al. 2012; Sharma et al. 2012). These developments are potentially significant because the radially averaged ratio t_{cool}/t_{ff} never approaches unity locally in central cluster galaxies, even when the atmosphere is cooling rapidly into molecular clouds and fueling star formation.

Understanding how thermally unstable cooling is triggered in clusters is essential because cold accretion likely plays a crucial role in the regulation of AGN feedback that may govern the growth of all massive galaxies (Pizzolato & Soker 2005; Gaspari et al. 2012, 2013; Li & Bryan 2014; Li et al. 2015; Voit & Donahue 2015; Voit et al. 2015). However, feedback involves complex physical interactions operating over many decades in scale, which is notoriously difficult to model. Nevertheless, modern, high-fidelity simulations have yielded predictions that can be tested using precision measurements, which is the focus of this paper.

The mechanism works generally as follows: thermally unstable cooling is assumed to occur when t_{cool}/t_{ff} falls below ∼10. The cooling gas then fuels both star formation and the AGN. As the radio AGN heats the atmosphere it lowers the central gas density, which in turn increases t_{cool} in response to AGN heating (e.g., Li et al. 2015; Voit & Donahue 2015). As the ratio t_{cool}/t_{ff} rises above 10, thermally unstable condensation ceases, cutting off the fuel supply for the AGN and quenching feedback. Over time, the atmosphere once again begins to cool.

Repeated episodes of heating and cooling are thought to maintain t_{cool}/t_{ff} above 10. However, a key and testable aspect of these models is that the minimum value of t_{cool}/t_{ff} in those systems experiencing a cooling episode should lie below 10. Simulation shows that a significant fraction of the population at any given time should be in a minimum state below 10 (e.g., Li et al. 2015). Furthermore, the ratio t_{cool}/t_{ff} at its minimum value should predict the onset of thermally unstable cooling, as traced by nebular emission, molecular clouds, and star formation, with greater certainty and lower observational scatter than the local cooling time alone (e.g., Rafferty et al. 2008). In other words, the additional physics associated with the denominator should act to decrease the scatter if local gravitational acceleration is playing a significant role. This issue was addressed by McNamara et al. (2016) who showed

that t_{ff} at the location of the t_{cool}/t_{ff} minimum spans only a narrow range of values in central galaxies. They further showed that the ratio t_{cool}/t_{ff} is driven almost entirely by t_{cool}. These results do not exclude a role for local acceleration, though they imply that some models are difficult to falsify. More significantly, they showed, as we do here, that the inner gas densities of cooling atmospheres vary over a strikingly small range in response to an enormous range of AGN power. The subtle response to AGN heating is difficult to model in most AGN feedback simulations.

Nonlinear cooling instabilities already in place would plausibly permit molecular clouds to form that would maintain the AGN feedback cycle without t_{cool}/t_{ff} falling near to or below 10 (Pizzolato & Soker 2005, 2010; Gaspari et al. 2017). Simulations have found that after initial large fluctuations the spherically averaged value of t_{cool}/t_{ff} in cluster atmospheres can stabilize above 10 while ongoing condensation occurs (e.g., Meece et al. 2015). Furthermore, chaotic cold accretion models (e.g., Gaspari et al. 2012, 2013, 2017) suggest that cooling may depend upon the local gas dynamical time, rather than the local free-fall time. Nonlinear instabilities driven by either large-scale turbulent motions in hot atmospheres, or smaller eddies, maintain gas condensation once the feedback cycle is initiated.

The narrow observed range of both densities and t_{ff} in cluster cores, in part, led McNamara et al. (2014, 2016) to suggest that thermally unstable cooling occurs when low-entropy gas from the cluster center is lifted in the updraft of buoyantly rising X-ray cavities. Furthermore, ALMA observations have shown that molecular gas in cluster cores lies preferentially in the wakes of buoyantly rising cavities (e.g., McNamara et al. 2014; Vantyghem et al. 2016; Russell et al. 2017). Whether the molecular gas is condensing directly from the uplifted hot gas, or whether the cold gas is being lifted directly, is unclear. However, indications are that at least some is cooling directly out of the hot atmosphere, at altitudes where the local value of t_{cool}/t_{ff} greatly exceeds 10. Moreover, numerical simulations have shown that marginally stable gas can be triggered to condense when uplifted by an AGN, indicating that this stimulated feedback mechanism is plausible at least (Revaz et al. 2008; Gaspari et al. 2012; Li & Bryan 2014; Brighenti et al. 2015; Voit et al. 2017; Yang & Reynolds 2016).

While the role of local acceleration in thermally unstable cooling is unclear, halo mass is clearly relevant to the AGN feedback cycle in clusters (e.g., Main et al. 2017). Hogan et al. (2017) developed techniques to determine cluster mass profiles across wide radial ranges that extend from cluster halos into the cores of the central galaxies. We adopt this methodology in this paper to calculate more accurate t_{cool}/t_{ff} profiles for a large sample of clusters, many of which are actively experiencing thermally unstable cooling. What differentiates this from preceding studies is careful attention to mass profile measurements within the central galaxy, and also to deprojected temperature and density measurements. We show that attention to these details is essential in order to test thermal instability and feedback models. We conclude that the role of local acceleration as captured by the minimum value of t_{cool}/t_{ff} is far less clear than has been previously understood.

The paper is arranged as follows. We describe our sample in Section 2, and data reduction in Section 3. In Section 4 we present thermodynamic and mass profiles for our clusters. Section 5 discusses density and entropy distributions, and in Section 6 we investigate what causes the onset of thermally

unstable gas cooling. Finally we discuss the possibility of a floor rather than a clear minimum in $t_{\rm cool}/t_{\rm ff}$ profiles in Section 7 before drawing conclusions in Section 8. Throughout this paper we have assumed a standard ΛCDM cosmology with: $\Omega_m = 0.3$, $\Omega_\Lambda = 0.7$, $H_0 = 70$ km s^{-1} Mpc^{-1}.

2. Sample Selection

2.1. Parent Sample

We aim to study the role that cluster mass plays in controlling the onset and magnitude of atmospheric cooling from the hot phase. To achieve this we require a sample of galaxy clusters that have been observed for tracers of cooling, and which have archival data available from the *Chandra X-ray Observatory* online repository.

Initially, we consider the 19 clusters observed for Hα in McDonald et al. (2010) that also have *Chandra* data.[10] These targets were selected to cover a large range in cluster richness and cooling rates. Deep *Magellan* observations were performed on this sample and hence the presence of multi-phase gas, as traced by Hα, is known for each of these clusters. To this sample we add 62 clusters that have been observed for the presence of molecular CO. These sources comprise the samples of Edge (2001) and Salomé & Combes (2003), in addition to a number of clusters that were observed since the publication of those papers (A. C. Edge 2017, private communication; see also Paper II). CO is a sensitive tracer of molecular gas and so the presence of significant cooling within these clusters is revealed by the detection, or not, of these lines (Paper II). The majority of these clusters have also been observed for Hα (Crawford et al. 1999; Cavagnolo et al. 2009; Rawle et al. 2012).

Basing our selection on clusters that have been observed for either CO or Hα, and which have been observed by *Chandra*, naturally biases us toward likely cool-core clusters. We therefore matched the 81 clusters within this initial sample to those of Hogan et al. (2015b) and the ACCEPT database (Cavagnolo et al. 2009) to see how many had previously been flagged as likely cool-core clusters due to their BCGs exhibiting optical emission lines (see Crawford et al. 1999; Cavagnolo et al. 2008). Only 11 of the 81 were expected to be non-cool-cores using this proxy. To ensure a well-sampled range of central cooling time we therefore added the 75 clusters from the ACCEPT database that are tagged as having been observed for Hα and which were not already included in our sample. Of these 75 clusters, 16 had Hα detections.

Our parent sample therefore consists of 156 clusters, of which 86 are expected to contain cool cores. The Hα coverage of these clusters is heterogeneous, and the presence of these lines is not a perfect indicator for the dynamic state of the cluster (Cavagnolo et al. 2008). However, by selecting our sample to have roughly equal numbers of line-emitting and non-line-emitting BCGs we should ensure a wide range of central cooling times is sampled.

During major mergers the dynamically dominant dark matter component of a cluster can become offset from the luminous X-ray atmosphere (e.g., the "Bullet Cluster"), making

X-ray-derived mass indicators unsuitable (Markevitch et al. 2002; Clowe et al. 2006). A number of clusters were therefore excluded as a result of clear major merger activity: A520 (the "train-wreck" cluster, Markevitch et al. 2005), A115 (Gutierrez & Krawczynski 2005), A2146 (Russell et al. 2010; White et al. 2015), A754 (Henry & Briel 1995; Macario et al. 2011). Additionally, A3158 is a late-stage merger (Wang et al. 2010) and its BCG is positioned on a chip-gap in the ACIS-I array, hence it was also removed from the sample. A further five sources were removed due to having unsuitable data (chip-placement, etc.).

2.2. Mass Sample

Thermally unstable cooling in cool-core clusters is typically confined to the central few tens of kpc, as shown by ALMA observations of cold gas (e.g., McNamara et al. 2014; Russell et al. 2014, 2016; Tremblay et al. 2016; Vantyghem et al. 2016). Furthermore the $t_{\rm cool}/t_{\rm ff}$ minimum is usually reported to occur at cluster-centric radii of 5–20 kpc (e.g., Gaspari et al. 2012; Voit et al. 2015; Hogan et al. 2017). High-resolution measurements are therefore required to constrain the minimum value of $t_{\rm cool}/t_{\rm ff}$. In Hogan et al. (2017) we demonstrated the importance of resolving these inner regions and deprojecting both density and temperature. This is one of the main contributing factors to the difference between our measured thermodynamic properties and those previously reported. However, the CLMASS models used to fit cluster mass (Nulsen et al. 2010, see Section 4.2) work best when the full extent of the cluster X-ray atmosphere is sampled. This places opposing redshift constraints on our sample: clusters must be close enough to sufficiently resolve the central ~10 kpc (criterion 1) while not being so close that their angular extent becomes greater than that observable by *Chandra* (criterion 2).

Figure 1 shows the distribution of available *Chandra* exposure times for our parent sample as a function of the angular scale at each cluster's redshift. Angular scale is plotted rather than redshift to allow a more direct view of resolvable scales. It was found in Hogan et al. (2017) that taking a minimum circular annulus of radius 3×0.492 arcsec pixels (roughly equivalent to the *Chandra* resolution), and then extending the radius of each successive annulus by one pixel (i.e., widths of 3, 4, 5, etc. pixels) provided good spatial sampling while ensuring more successful deprojection. Using these resolution-based annuli as a guide, we show in Figure 1 three vertical solid lines. The leftmost line shows the angular scale at which the three smallest annuli would fall within 10 kpc. The middle line shows where the two innermost annuli would cover 10 kpc radially, and the rightmost line where the innermost annulus alone would cover 10 kpc. These lines act only as a rough guide since count rate and the presence (or not) of an AGN will place additional constraints on how many radial bins can provide usable spectra in the cluster center.

The maximum cluster field-of-view is difficult to constrain as it depends on the exact observational set-up used as well as the position of the cluster on the ACIS array. Multiple pointings of a single cluster can also change the available scale. As an approximate guide we assume that a circular region of ~690″ radius is recoverable, roughly equivalent to the maximum extent of the ACIS-I array. Three vertical dotted lines are shown on Figure 1. These correspond to the angular scale (redshift) at which this maximum angular size

---

[10] McDonald et al. (2010) identify Abell 1837 as having been observed by *Chandra*. These data are not apparent in the archive, although an *XMM* observation of this target exists. However, since publication of McDonald et al. (2010), data for Abell 970 has become available and hence the total remains at 19.
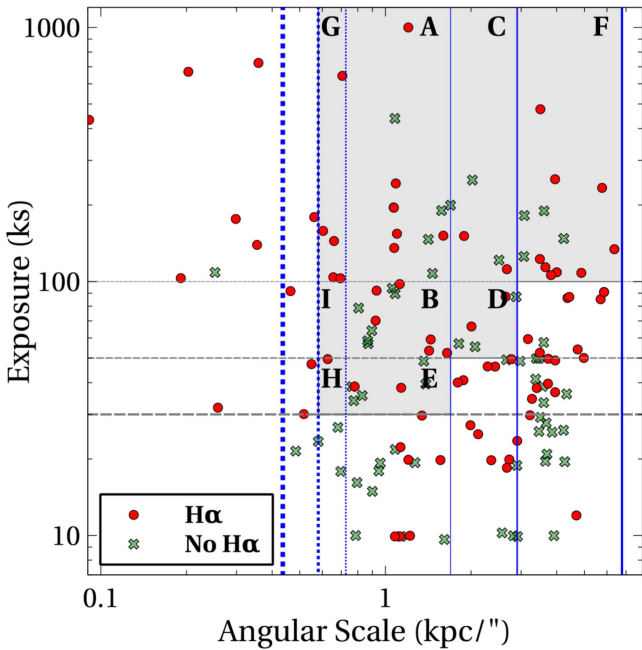
Figure 1. Distribution of the *Chandra* exposures available for our parent sample as a function of angular scale on the sky at each cluster's redshift. Clusters whose BCGs exhibit Hα are shown as red circles, those without as green crosses. The three dashed vertical lines represent limits at which 300, 400, and 500 kpc (left to right) can be recovered for typical cluster placement on the ACIS-I array. The vertical solid lines show the limits at which 3, 2, and 1 (left to right) annular temperature measurements are reasonable within 10 kpc. Horizontal lines at 30, 50, and 100 ks total *Chandra* exposures are also shown. This grid creates various regions within which clusters have comparable resolution and depth. We highlight the regions from which our mass sample have been taken, with labelled boxes corresponding to regions in Table 1. Further details are given in the text.

corresponds to a recoverable physical scale of radius 300 (left), 400 (middle), and 500 kpc (right).

As well as spatial constraints, we also desire adequate counts to extract suitable spectra. We therefore finally show three horizonal dashed lines on Figure 1 at raw *Chandra* exposure times of 30, 50, and 100 ks. The count rate of each observation could equivalently be used here, although these can be affected by strong point sources and substructures. Count rate is also likely to disfavor non-cool-core clusters, so raw exposure is used as a proxy for depth of observation.

The various constraints plotted in Figure 1 create a grid of nine regions that we label A–I. Note that region I contains no sources. The lone source in region H (A2634) was from the sample observed for CO but was found to be an isolated elliptical and thus removed from the sample. The 57 clusters within the shaded region provide a reasonable compromise between physical resolution and recoverable angular scales while having the deepest data. Of these clusters, 33 are line-emitting. These clusters constitute our mass sample and are listed in Table 1.

3. Data Reduction

Data reduction was performed using CIAO version 4.7 with CALDB version 4.6.7 (Fruscione et al. 2006) following the methods described in Hogan et al. (2017). A brief outline is given here.

Available imaging data were downloaded from the online *Chandra* repository. Level-1 events were filtered and

reprocessed to correct for charge transfer inefficiencies and time-dependent gains. VFAINT mode was used for more accurate filtering when available. The LC_CLEAN script by M. Markevitch was used to remove periods suffering from background flares. In instances of multiple pointings to a single source, the separate ObsIDs were reprojected to a common position. Blank-sky backgrounds were processed in an identical manner for each observation and normalized to the corresponding 9.5–12.0 keV flux. A background and point-spread-function-corrected 0.5–7.0 keV image was created for each cluster. This was used to identify point sources and clearly non-equilibrium atmospheric structures such as cavities and filaments. These were masked out from subsequent analysis. The strucure identification was done using the WAVDETECT (Freeman et al. 2002) algorithm supplemented by manual inspection in DS9 (Joye & Mandel 2003).

3.1. Spectral Extraction

As mentioned in Section 2.2 (see also Hogan et al. 2017), we require deprojected densities and temperatures for robust determination of t_{cool} and related quantities. Retaining sufficient counts after deprojection to measure temperature often requires that spectra be extracted from large regions. However, we ideally want to sample t_{cool}/t_{ff} at altitudes $\lesssim 10$ kpc and so small central annular regions are desirable. These opposing requirements lead us to extract two separate sets of concentric circular annuli for each cluster. The first is a set of 16 annuli identical to those used and described in Hogan et al. (2017), with radii dictated solely by angular resolution (see also Section 2.2). These annuli provide the highest reasonable radial sampling but for many clusters the small central annular regions may contain insufficient counts for successful spectral fitting. This is particularly prevalent in non-cool-cores with hot diffuse central atmospheres. We therefore extract a second set of annuli for each cluster, where the central region is defined to include a set number of counts. The exact number of counts per annulus varies by cluster. This limit again requires a compromise: too few counts and there is less likelihood of successful fitting; too many counts and the radial binning becomes uselessly large and/or there are too few bins to recover a practical profile.

There is no strict limit on the number of counts required to successfully fit (de)projected temperatures, although hotter clusters typically need more. We set 3000 counts as the hard minimum required per spectral region. A single central region of radius <10 kpc with more counts is preferred to multiple regions <10 kpc each with fewer counts. Practically, it was found that all expected cool-core clusters in our sample could have at least one annulus within ~ 10 kpc containing $\gtrsim 4500$ counts, Often a central annulus <10 kpc and with $\gtrsim 8000$ counts was possible. Non-line-emitting clusters have lower surface brightness peaks, thus fewer counts centrally. Among these, larger central annuli (radii ~ 20–30 kpc) were used in a number of cases to ensure that our minimum count limit of 3000 was not breached. However these clusters lack nebular emission, indicating that their atmospheres are not cooling and are thus expected to have high central cooling times. The loss of radial resolution of their various parameter profiles (e.g., t_{cool}, entropy) is therefore acceptable and should not impact our results.

Two sets of spectra were therefore extracted for each cluster, one from each of the two sets of annular regions described

Table 1
Chandra Data Used in Our Analysis

Cluster	z	Scale (kpc/″)	ObsIDs	Total Exposure Raw (ks)	Total Exposure Cleaned (ks)	N_H (10^{22} cm^{-2})	Cluster Center R.A. (J2000)	Cluster Center Decl. (J2000)
Region A								
A85	0.0551	1.071	904, 15173, 15174, 16263, 16264	195.240	193.64	0.039	00:41:50.476	−09:18:11.82
A133	0.0566	1.098	13518, 9897, 2203	154.279	141.058	0.0153	01:02:41.594	−21:52:53.65
A401	0.0745	1.415	14024, 2309	146.637	145.260	0.0988	02:58:57.862	+13:34:58.25
Hydra A	0.0550	1.069	4969, 4970	195.734	163.79	0.043	09:18:05.681	−12:05:43.51
A1650	0.0838	1.575	4178, 5822, 6356, 6357, 6358, 7242, 7691	190.330	167.164	0.013	12:58:41.485	−01:45:40.82
A1795	0.0625	1.204	493, 3666, 5286, 5287, 5288, 5289, 5290, 6159, 6160, 6161, 6162, 6163, 10898, 10899, 10900, 10901, 12027, 12028, 12029, 13106, 13107, 13108, 13109, 13110, 13111, 13112, 13113, 13412, 13413, 13414, 13415, 13416, 13417, 14268, 14269, 14270, 14271, 14272, 14273, 14274, 14275, 15485, 15486, 15487, 15488, 15489, 15490	666.530	625.500	0.041	13:48:52.521	+26:35:36.30
A2029	0.0773	1.464	891, 4977, 6101	107.637	103.31	0.033	15:10:56.077	+05:44:41.05
A2142	0.0909	1.694	15186, 16564, 16565, 5005	199.709	182.308	0.0431	15:58:19.906	+27:13:59.36
Cygnus A	0.0561	1.088	(359), 360, (1707), 5830, 5831, 6225, 6226, 6228, 6229, 6250, 6252	243.320	228.251	0.28	19:59:28.316	+40:44:01.99
A3667	0.0556	1.080	5751, 5752, 5753, 6292, 6295, 6296	438.468	399.133	0.0445	20:12:41.710	−56:51:24.17
A2597	0.0852	1.598	922, 7329, 6934	151.639	134.817	0.0246	23:25:19.720	−12:07:27.62
A2626	0.0553	1.074	16136, 3192	135.621	132.487	0.0383	23:36:30.432	+21:08:47.23
Region B								
A119	0.0442	0.870	4180, 7918	56.971	55.947	0.0352	00:56:16.088	−01:15:20.37
A160	0.044	0.866	3219	58.491	51.326	0.0406	01:12:59.749	+15:29:28.53
A3112	0.0761	1.443	13135, 2516	59.164	51.832	0.0133	03:17:57.654	−44:14:17.97
A478	0.0881	1.647	1669, 6102	52.390	46.763	0.281	04:13:25.291	+10:27:55.15
A3376	0.0456	0.896	3202, 3450	64.115	62.070	0.0498	06:02:10.700	−39:57:37.05
A1644	0.0471	0.924	2206, 7922	70.199	70.035	0.0413	12:57:11.564	−17:24:34.76
Zw8276	0.075	1.424	11708, 8267	53.474	53.474	0.0383	17:44:14.453	+32:59:29.41
A2319	0.0557	1.082	3231, 15187	89.600	86.793	0.0810	19:21:10.110	+43:56:44.20
AS1101	0.058	1.123	11758	97.735	92.573	0.039	23:13:58.693	−42:43:38.58
A2589	0.0407	0.805	6948, 7190, 7340	78.666	78.439	0.0316	23:23:57.356	+16:46:38.55
A4059	0.0475	0.931	5785	92.121	87.938	0.012	23:57:00.473	−34:45:33.04
Region C								
PKS 0745−191	0.1028	1.890	12881, 2427, 6103, 7694	151.189	148.629	0.415	07:47:31.291	−19:17:40.02
A1413	0.1427	2.508	1661, (5002), 5003	121.456	106.103	0.0183	11:55:17.991	+23:24:19.82
A2034	0.111	2.022	12885, 12886, 13192, 2204	250.951	226.072	0.0154	15:10:11.556	+33:30:40.53
Hercules A	0.154	2.672	1625, 5796, 6257	111.86	108.792	0.06	16:51:08.203	+04:59:32.51
Region D								
RX J0821+07	0.110	2.006	17194, 17563	66.559	63.488	0.0195	08:21:02.242	+07:51:48.99
A1201	0.1688	2.881	4216, 9616	87.061	63.581	0.0157	11:12:54.536	+13:26:07.75
A2069	0.1138	2.066	4965	55.417	46.198	0.0192	15:24:07.476	+29:53:17.42
A2204	0.1522	2.646	7940, 499	87.210	80.563	0.061	16:32:46.887	+05:34:31.42
A2244	0.0980	1.812	4179	56.965	53.894	0.0188	17:02:42.357	+34:03:36.51
Region E								
A399	0.0716	1.365	3230	48.631	46.328	0.106	02:57:53.124	+13:01:51.09
A576	0.0385	0.763	3289	38.592	27.737	0.055	07:21:30.162	+55:45:41.71
A744	0.0729	1.387	6947	39.519	34.596	0.0343	09:07:20.481	+16:39:04.56
NGC 5098	0.0394	0.780	6941	38.623	38.623	0.0131	13:20:14.728	+33:08:36.15
A3571	0.0391	0.774	4203	33.987	15.680	0.0425	13:47:28.599	−32:51:54.71

Table 1
(Continued)

Cluster	z	Scale (kpc/″)	ObsIDs	Total Exposure		N_H (10^{22} cm^{-2})	Cluster Center	
				Raw (ks)	Cleaned (ks)		R.A. (J2000)	Decl. (J2000)
A1991	0.0587	1.136	3193	38.305	34.526	0.0234	14:54:31.554	+18:38:38.29
A2107	0.042	0.829	4960	35.573	34.805	0.0445	15:39:39.043	+21:46:58.55
Region F								
MS 0735+7421	0.216	3.503	10468, 10469, 10470, 10471 10822, 10918, 10922	476.700	446.943	0.0328	07:41:44.205	+74:14:38.31
A665	0.1824	3.067	12286, 13201, 3586	125.528	108.598	0.0433	08:30:58.622	+65:50:24.49
4C+55.16	0.242	3.817	1645, 4940	106.030	70.488	0.0449	08:34:54.845	+30:20:59.43
Zw2701	0.215	3.490	12903, 3195	122.685	117.568	0.00751	09:52:49.161	+51:53:05.58
A1689	0.1832	3.078	1663, 5004, 6930, 7289	181.857	165.773	0.0183	13:11:29.512	−01:20:28.03
A1758	0.279	4.233	13997, 15538, 15540	147.696	129.722	0.0103	13:32:48.548	+50:32:32.71
MACS 1347-11	0.451	5.767	13516, 13999, 14407, 3592, 506, 507	233.800	204.415	0.046	13:47:30.582	−11:45:09.21
A1835	0.2532	3.947	6880, 6881, 7370, 495, 496	252.740	204.217	0.020	14:01:02.080	+02:52:42.99
MACS 1423+24	0.543	6.370	1657, 4195	134.095	121.766	0.022	14:23:47.870	+24:04:42.50
Zw7160	0.2578	3.999	4192, 543, 7709	108.804	92.179	0.0318	14:57:15.104	+22:20:33.89
MACS 1532+30	0.343	4.875	14009, 1649, 1665	108.198	102.191	0.023	15:32:53.747	+30:20:59.43
A2219	0.2248	3.611	13988, 14355, 14356, 14431, 14451, 896	189.741	173.443	0.0176	16:40:19.822	+46:42:41.19
A2390	0.228	3.650	(500), (501), 4193	113.94	71.647	0.079	21:53:36.792	+17:41:44.25
Region G								
RX J0338+09	0.0349	0.695	7939, 919, 9792	103.012	91.748	0.176	03:38:40.597	+09:58:12.54
A496	0.0329	0.656	931, 3361+, 4976	104.002	62.750	0.040	04:33:37.932	−13:15:40.59
A2052	0.0355	0.706	890, 5807, 10477, 10478, 10479, 10480, 10879, 10914 , 10915, 10916, 10917	644.990	640.429	0.027	15:16:44.484	+07:01:17.86
A2199	0.0302	0.605	10748, 10803, 10804, 10805 , 10804, 10805	119.870	119.610	0.039	16:28:38.245	+39:33:04.21
IC1262	0.0331	0.660	2018, 6949, 7321, 7322	144.430	130.164	0.0178	17:33:01.973	+43:45:35.13

Note. Columns are: (i) cluster name, (ii) redshift, (iii) angular scale on the sky at the given redshifts using standard cosmology, (iv) observation IDs used for the analysis, (v) raw combined exposure of the ObsIDs used, (vi) useable exposure after data filtering, (vii) (fixed) column density used in fitting, (viii) R.A., (ix) decl. Sources are presented sorted into regions corresponding to those described in Section 2, then arranged by R.A. within each region.

above. The CIAO tasks MKACISRMF and MKWARF were respectively used to create individual redistribution matrix files and auxillary response files for each spectrum, and exposure maps created to correct each observation for lost area. Spectra were binned to ensure 30 counts per channel. In instances of clusters having multiple observations, spectra were extracted and treated separately for each ObsID. Since these could be separated greatly in time they were not summed but instead later loaded and fitted simultaneously within the modeling package XSPEC (Arnaud 1996).

4. Results and Mass Profiles

4.1. Thermodynamic Properties of Hot Atmospheres

4.1.1. Projected Profiles

We initially calculate projected thermodynamic profiles, which provide a base from which the effects of deprojection on the final values of t_{cool}/t_{ff} can be understood.

The extracted spectra and corresponding response files were loaded into XSPEC version 12.8.2 for spectral fitting (Arnaud 1996). We fitted the spectra with an absorbed single temperature (PHABS*MEKAL) model (Mewe et al. 1985;

Balucinska-Church & McCammon 1992; Liedahl et al. 1995), which was found in Hogan et al. (2017) to give a good description of atmospheres across our radii of interest. Solar abundances were set to those of Anders & Grevesse (1989), and line-of-sight galactic extinctions were frozen to values taken from the LAB survey (Kalberla et al. 2005), unless the best fit was found to be significantly different. For each cluster, preference was given to the set of annuli with finer central radial sampling. However, sometimes this resolution-based binning left too few counts in the central few spectra to obtain convergent fits. In these cases we instead used the set of count-based annuli to recover profiles for various atmospheric properties. Regardless of which set of annuli were used, convergent fits were sometimes not possible for the smallest radial bins, most often in non-cool-core clusters. In these instances, multiple central regions could be combined. However, we opted against this since fits over very large central regions where the temperature may be rapidly changing can bias high subsequent measures of central cooling and entropy (Panagoulia et al. 2014; Hogan et al. 2017). Instead we truncated our subsequent profiles at the smallest radial annulus to which a stable spectral fit is recovered.
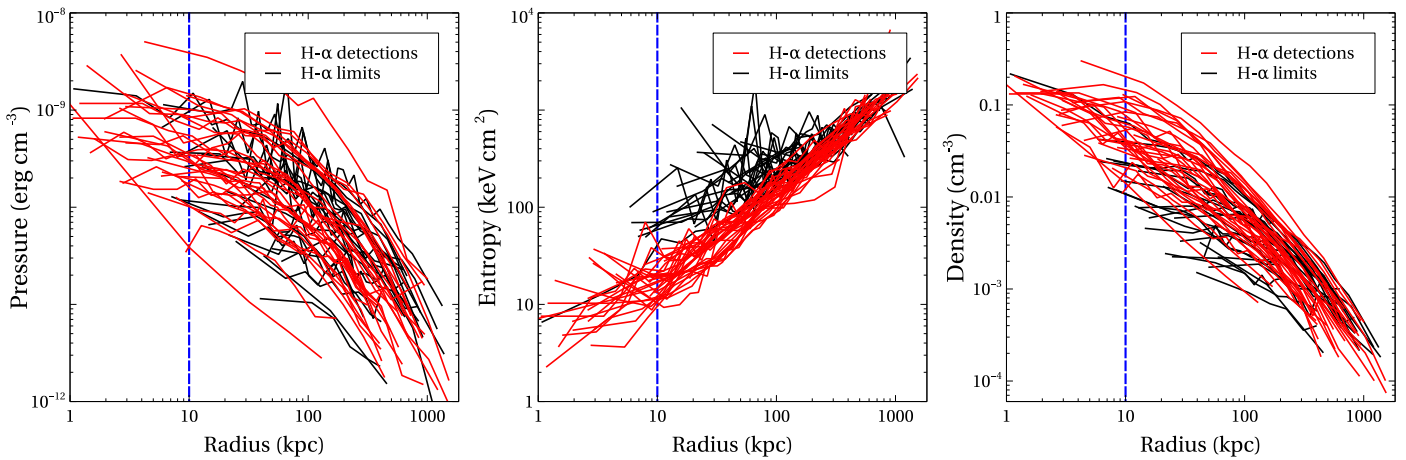
Figure 2. Deprojected pressure, entropy, and density profiles for our sample, colorized by the presence or not of nebular Hα emission. Note that while the uncertainty of deprojecting the more diffuse non-line-emitting clusters is apparent in these plots, clear trends can still be recovered. In particular note the lower central entropies of line-emitting clusters (see Section 5.2). Error bars have been removed for clarity.

Temperatures and normalizations from the fitted models were used to derive projected electron number densities n_e

$$n_e = D_A(1 + z)10^7 \sqrt{\frac{N\,4\,\pi\,1.2}{V}} \quad (1)$$

where N is the model normalization, D_A is the angular distance to the source, and V the volume of a spherical shell bounded by the inner and outer projected annulus edges. The factor of 1.2 arises from the relative abundances of electron n_e to ion n_H number density (Anders & Grevesse 1989). Cooling times were calculated using

$$t_{\text{cool}} = \frac{3\,P}{2\,n_e\,n_H\,\Lambda(Z, T)} = \frac{3PV}{2L_X} \quad (2)$$

where P is pressure ($P = 2n_e k_B T$), and $\Lambda(Z, T)$ the cooling function for gas at a specific abundance Z and temperature T. The bolometric X-ray luminosity L_X is found by integrating the fitted model between 0.1 and 100 keV. We finally calculated the specific entropy ($K = kT\, n_e^{-2/3}$) of the atmosphere, which provides an imprint of the thermal history of a cluster (Panagoulia et al. 2014).

4.1.2. Deprojected Profiles

Spectra extracted from the inner regions of a cluster are contaminated by projected emission from higher altitudes. An accurate measure of the inner cluster properties therefore requires deprojection of the spectra to remove this super-posed emission. The model-independent DSDEPROJ routine is used to deproject our spectra (Russell et al. 2008, also see Sanders & Fabian 2007, 2008). Absorbed single temperature (PHABS*MEKAL) models are fitted to the deprojected spectra, as for the projected spectra.

Deprojected density, pressure, and entropy profiles are presented in Figure 2, colorized by the detection or not of Hα emission (Crawford et al. 1999; Cavagnolo et al. 2009; Rawle et al. 2012). Deprojected densities are typically 10%–50% lower than the equivalent projected values.

4.2. Mass Profiles

A major source of uncertainty when comparing cooling models to data concerns the difficulty of observationally measuring the dynamical times of the cooling gas. The simplest dynamical timescale, and one on which many cooling models rely, is the free-fall time t_{ff}. This timescale relies only on the enclosed mass and is commonly approximated as

$$t_{\text{ff}} = \sqrt{\frac{2\,r}{g}} \quad (3)$$

(e.g., Gaspari et al. 2012; McDonald et al. 2015), where g is the standard gravitational acceleration. Free-fall time is difficult to measure for any sizeable sample of galaxy clusters, particularly at the low altitudes where it is believed to be most important in the context of cooling instabilities (e.g., McCourt et al. 2012; Sharma et al. 2012). Hydrostatic mass estimates at $\lesssim 10$ kpc are possible for only the most nearby clusters (e.g., M87, see, Romanowsky & Kochanek 2001; Russell et al. 2015). Stellar velocity dispersions can be used to infer the enclosed gravitating mass within the central galaxy, although these are only available for a minority of BCGs. In Hogan et al. (2017) we presented a method for calculating cluster mass profiles across a wide radial range. This is done for our current sample, and the mass profiles subsequently used to calculate t_{ff}. A brief outline of the method is given here.

4.2.1. Cluster Mass Profiles

Our mass profiles contain two components: an NFW component to account for the majority of the cluster mass on large scales, and an isothermal sphere to account for the stellar mass of the BCG. We initially obtain isophotal radii r_{k20} and apparent K-band magnitudes m_{k20} from 2MASS (Skrutskie et al. 2006) for the BCG in each cluster. These are extinction, evolution, and K-corrected (Poggianti 1997; Schlegel et al. 1998), then converted to enclosed stellar masses within r_{k20} (Bell et al. 2003; Baldry et al. 2008). An *equivalent stellar velocity dispersion* σ_* is calculated for each of these masses from Pizzella et al. (2005), which describes the isothermal

potential

$$\Phi_{\mathrm{iso,c}}(r) = \sigma_*^2 \ln(1 + (r/r_{\mathrm{I}})^2), \qquad (4)$$

where r_{I} is an isothermal scale radius. This form of isothermal potential is used for numerical reasons. In practice r_{I} is set to an arbitrarily small but non-zero value ($\ll 1$ kpc) so the isothermal potential is equivalent to that of a basic singular isothermal sphere, $\Phi_{\mathrm{iso}}(r) = 2\sigma^2 \ln(r)$, at all radii of interest.

Based on the methods of Main et al. (2017), we use the CLMASS (Nulsen et al. 2010) package of cluster mass mixing models to fit an ISONFWMASS model to the *Chandra* data. This model combines an isothermal potential (Equation (4)) with an NFW potential,

$$\Phi_{\mathrm{NFW}}(r) = -4\pi G \rho_0 \, r_{\mathrm{s}}^2 \, \frac{\ln(1 \, + \, r/r_{\mathrm{s}})}{r/r_{\mathrm{s}}} \qquad (5)$$

where r_{s} is scale radius. We fix the isothermal potential to that calculated for the stellar component of the BCG, meaning that the remaining cluster mass is fitted with the NFW. In Hogan et al. (2017) we found this method to provide reliable cluster mass estimates from small ($\gtrsim 1$ kpc) radii up to R_{2500}. Model parameters and cluster masses for our sample are presented in Table 2. As a sanity check, total cluster masses (M_{2500}) were compared to other published values where available (e.g., Vikhlinin et al. 2006, 2009; Allen et al. 2008; Main et al. 2017). Good overall agreement was found. Notes on some individual clusters can be found in Appendix A.

For our sample, the mean of the equivalent stellar velocity dispersions is 268.9 ± 7.7 km s^{-1}, with a standard deviation of 58.3 km s^{-1}. As this stellar component is a major contributor to the acceleration at the altitudes where $(t_{\mathrm{cool}}/t_{\mathrm{ff}})_{\mathrm{min}}$ is typically found, the large range shows that individually tailored inner mass profiles are required for accurate estimates of $(t_{\mathrm{cool}}/t_{\mathrm{ff}})_{\mathrm{min}}$.

4.2.2. Differences from Hogan et al. (2017)

Our approach here is slightly different from that of Hogan et al. (2017). The CLMASS models contain a switch to allow the inclusion of a β-model component in the cluster mass profile to account for emission outside of the field of view (also see Section 2.2). Typically this switch is turned off, which gives more stable fits. In order to avoid underestimating the cluster mass by missing emission beyond the field of view, a mass model with the β parameter set free was fitted and the result compared to the original model. An F-test was used to determine whether the β-model provided a better fit. We found that a β-model was justified for only five clusters (A133, A401, A1991, A1758, A2052: see Table 2).

A further issue not encountered in Hogan et al. (2017) was that four clusters (A665, MACS 1347−11, MACS 1423+24, and MACS 1532+30) are at high enough redshift that their BCGs are undetected in 2MASS. These are all found in Region F of Figure 1 and so typically have only a single region within the innermost region where the isothermal component is expected to dominate ($\lesssim 10$ kpc). We take the mean σ_* of all clusters in Region F with a 2MASS-detected BCG, and adopt this value as an estimate of the isothermal component for these four clusters and then fitted them similarly to the others.

5. Discussion

5.1. Density Distribution Requires Gentle AGN Feedback

Several features are noteworthy in Figure 2. First, deprojection was less successful for clusters without nebular emission (i.e., non-cool-cores). These systems can typically only have their properties traced to higher altitudes because their atmospheres are more diffuse, disturbed, and fainter. Nevertheless, interesting trends are seen.

The left-hand panel of Figure 2 shows no clear difference between the atmospheric pressures of cooling and non-cool-core clusters. However, the entropy profiles of cool-core and non-cool-core clusters (middle panel) segregate, confirming the threshold discovered by Rafferty et al. (2008) and Cavagnolo et al. (2008). The single Hα non-emitting low entropy cluster is A2029, a well known anomaly (see e.g., McNamara et al. 2016). The entropy dichotomy is a consequence of higher central temperatures and lower central densities of non-cool-core clusters, and the converse (right-hand panel, Figure 2).

Significantly, the spread of atmospheric gas density is relatively small at all radii in cool-core clusters (see Figure 2). Most of this spread correlates with halo mass. However, most feedback models indicate that density profiles vary throughout the AGN activity cycle. To account for the dependence on cluster mass, in Figure 3 the density profiles of the Hα emitting clusters were renormalized to the median density at 100 kpc, i.e., by a factor of $\rho_{\mathrm{median}}(100\,\mathrm{kpc})/\rho(100\,\mathrm{kpc})$. This normalization further reduces the spread in observed inner densities. The remaining spread can now be understood as the scatter caused by AGN feedback and other local atmospheric inhomogeneities.

The observed range in central density is strikingly smaller than some simulations suggest. We find no evidence for the large variations in gas density expected if the radially averaged $t_{\mathrm{cool}}/t_{\mathrm{ff}}$ were varying in response to AGN heating and radiative cooling cycles. In particular, we see no evidence that $t_{\mathrm{cool}}/t_{\mathrm{ff}}$ is rising and falling above and below 10. Outbursts violent enough to quickly raise $t_{\mathrm{cool}}/t_{\mathrm{ff}}$ back above 10 would cause greater than order-of-magnitude swings in density at the cluster center ($\lesssim 20$ kpc, e.g., Sijacki & Springel 2006; Li et al. 2015; Prasad et al. 2015), which are not observed. Restricting our analysis to those clusters with Hα emission (i.e., cool-core clusters) we find a 10–90th percentile spread in central gas density only factors of 1.2–1.5 wider at 10 kpc than at higher altitudes ($\gtrsim 100$ kpc, see Figure 2) where AGN feedback should be less efficient. The expected spread in densities at 10 kpc due to heating and cooling cycles in precipitation-based models is expected to be one to two orders of magnitude greater (e.g., Li et al. 2015). Our sample spans four decades in AGN power, from relatively weak ($\sim$few 10^{42} erg s^{-1}) sources such as NGC 5098 and the BCG in A1644, to the most powerful cavity system known, MS 0735+7421 ($\sim 10^{46}$ erg s^{-1}). The small range of central densities shows that central atmospheres do not experience large density swings in response to radio-AGN feedback.

In keeping with other studies, we have derived radially averaged quantities. Our density measurements represent volume-averaged, spectroscopic quantities. Our analysis is insensitive to cooler inhomogeneities mixed into the atmosphere but no longer emitting in the X-ray band. Colder and denser gas phases traced by nebular and CO emission are usually present in the central region of the clusters studied here.

Table 2
Details of the ISONFWMASS Profile Fits

Cluster	Lines?	σ_* (km s^{-1})	$\rho_{0,ISO}$ (keV)	Beta	$R_{s,NFW}$ (arcmin)	$\rho_{0,NFW}$ (keV)	R_{2500} (kpc)	M_{2500} ($\times 10^{14} M_\odot$)
Region A								
A85	LE	270.4 ± 6.4	0.450	…	$7.37^{+0.46}_{-0.21}$	$49.24^{+1.64}_{-0.92}$	516.7	$2.07^{+0.04}_{-0.03}$
A133	LE	249.1 ± 7.6	0.382	0.60	$13.86^{+1.18}_{-0.74}$	$64.90^{+3.80}_{-1.71}$	519.6	$2.10^{+0.08}_{-0.09}$
A401	NLE	280.3 ± 8.8	0.486	0.50	$7.53^{+0.30}_{-0.16}$	$73.18^{+1.30}_{-2.96}$	565.1	$2.82^{+0.10}_{-0.10}$
Hydra A	LE	236.6 ± 8.4	0.344	…	$5.85^{+1.52}_{-0.49}$	$32.29^{+1.52}_{-1.55}$	423.6	$1.14^{+0.03}_{-0.04}$
A1650	NLE	236.1 ± 12.4	0.343	…	$3.11^{+0.11}_{-0.15}$	$46.64^{+0.80}_{-0.78}$	506.2	$2.00^{+0.07}_{-0.06}$
A1795	LE	221.1 ± 6.5	0.302	…	$7.45^{+0.25}_{-0.25}$	$57.29^{+1.18}_{-1.25}$	539.3	$2.37^{+0.03}_{-0.04}$
A2029	NLE	335.9 ± 10.0	0.694	…	$6.79^{+0.49}_{-0.46}$	$88.68^{+4.84}_{-4.10}$	686.1	$4.94^{+0.17}_{-0.19}$
A2142	NLE	241.2 ± 11.3	0.360	…	$14.67^{+1.58}_{-0.16}$	$156.47^{+13.92}_{-2.00}$	753.2	$6.63^{+0.46}_{-0.39}$
Cygnus A	LE	268.5 ± 7.5	0.446	…	$2.43^{+0.22}_{-0.18}$	$48.44^{+1.26}_{-0.82}$	525.8	$2.18^{+0.06}_{-0.06}$
A3667	NLE	262.3 ± 7.6	0.426	…	$17.36^{+1.19}_{-0.59}$	$50.46^{+2.25}_{-0.52}$	418.1	$1.10^{+0.14}_{-0.13}$
A2597	LE	217.7 ± 10.4	0.293	…	$2.86^{+0.15}_{-0.08}$	$36.63^{+1.41}_{-0.59}$	452.3	$1.43^{+0.03}_{-0.03}$
A2626	LE	243.3 ± 7.3	0.366	…	$2.56^{+0.08}_{-0.13}$	$18.51^{+0.25}_{-0.38}$	344.5	$0.61^{+0.14}_{-0.14}$
Region B								
A119	NLE	237.9 ± 5.4	0.350	…	$4.49^{+3.53}_{-3.83}$	$17.58^{+3.16}_{-14.98}$	333.1	$0.58^{+0.08}_{-0.08}$
A160	NLE	207.3 ± 7.3	0.266	…	$2.07^{+0.35}_{-0.58}$	$11.93^{+0.41}_{-0.46}$	280.1	$0.33^{+0.02}_{-0.02}$
A3112	LE	266.2 ± 8.5	0.438	…	$7.50^{+0.63}_{-0.84}$	$66.70^{+4.39}_{-61.48}$	570.5	$2.84^{+0.14}_{-0.15}$
A478	LE	271.1 ± 7.0	0.455	…	$7.10^{+0.17}_{-0.24}$	$86.66^{+1.75}_{-1.73}$	647.0	$4.19^{+0.59}_{-0.66}$
A3376[a]	NLE	198.5 ± 7.0	0.01^a(0.244)	…	$14.99^{+7.32}_{-1.10}$	$24.36^{+7.02}_{-2.10}$	263.1	$0.27^{+0.03}_{-0.03}$
A1644	LE	248.5 ± 6.6	0.382	…	$6.11^{+1.98}_{-1.83}$	$10.67^{+2.64}_{-2.32}$	258.3	$0.26^{+0.03}_{-0.03}$
Zw8276	LE	218.0 ± 7.1	0.294	…	$3.35^{+0.33}_{-0.33}$	$36.78^{+1.97}_{-1.23}$	454.6	$1.43^{+0.05}_{-0.05}$
A2319	NLE	249.1 ± 6.5	0.384	…	$9.91^{+0.91}_{-1.50}$	$81.22^{+4.55}_{-8.35}$	642.1	$3.97^{+0.24}_{-0.23}$
AS1101	LE	219.1 ± 7.5	0.297	…	$2.77^{+0.12}_{-0.08}$	$21.82^{+0.46}_{-0.22}$	364.6	$0.73^{+0.01}_{-0.01}$
A2589	NLE	220.2 ± 6.3	0.300	…	$6.38^{+0.44}_{-0.68}$	$27.47^{+1.15}_{-1.61}$	398.7	$0.94^{+0.03}_{-0.03}$
A4059	LE	244.3 ± 5.7	0.369	…	$4.33^{+0.43}_{-0.61}$	$29.98^{+1.13}_{-1.89}$	425.6	$1.15^{+0.05}_{-0.04}$
Region C								
PKS 0745−191	LE	289.8 ± 14.3	0.519	…	$4.32^{+0.23}_{-0.38}$	$75.38^{+1.71}_{-3.65}$	629.1	$3.91^{+0.10}_{-0.10}$
A1413[b]	NLE	363.7 ± 12.4	0.818	…	$5.77^{+0.15}_{-0.03}$	$98.51^{+0.66}_{-2.77}$	660.0	$4.70^{+0.15}_{-0.15}$
A2034[a]	NLE	276.6 ± 10.8	0.01^a(0.473)	…	$31.69^{+14.31}_{-1.87}$	$283.09^{+122.52}_{-17.31}$	699.4	$5.41^{+0.59}_{-0.54}$
Hercules A	LE	284.7 ± 13.9	0.501	…	$0.91^{+0.01}_{-0.10}$	$27.48^{+0.58}_{-0.92}$	395.7	$1.02^{+0.03}_{-0.04}$
Region D								
RX J0821+07	LE	246.7 ± 8.9	0.376	…	$1.56^{+0.53}_{-0.48}$	$21.48^{+2.45}_{-1.99}$	357.7	$0.72^{+0.06}_{-0.07}$
A1201	NLE	338.1 ± 12.8	0.707	…	$10.35^{+2.33}_{-2.35}$	$81.06^{+15.51}_{-16.69}$	446.6	$1.50^{+0.14}_{-0.13}$
A2069[a]	NLE	262.8 ± 10.0	0.01^a(0.427)	…	$2.91^{+0.89}_{-0.68}$	$19.12^{+1.66}_{-2.22}$	323.7	$0.54^{+0.04}_{-0.05}$
A2204	LE	343.3 ± 13.0	0.729	…	$1.25^{+0.14}_{-0.19}$	$78.54^{+1.80}_{-2.34}$	639.7	$4.32^{+0.16}_{-0.15}$
A2244	NLE	288.1 ± 8.5	0.513	…	$3.58^{+0.43}_{-0.36}$	$45.77^{+2.93}_{-2.26}$	501.0	$1.96^{+0.07}_{-0.07}$
Region E								
A399	NLE	269.0 ± 8.9	0.448	…	$3.91^{+0.43}_{-0.98}$	$39.71^{+2.59}_{-4.44}$	478.2	$1.66^{+0.10}_{-0.10}$
A576	NLE	224.9 ± 4.5	0.313	…	$15.62^{+4.41}_{-4.45}$	$42.05^{+9.67}_{-9.55}$	431.3	$1.18^{+0.15}_{-0.13}$
A744	NLE	247.3 ± 6.6	0.378	…	$1.12^{+0.35}_{-0.19}$	$12.03^{+1.49}_{-0.90}$	285.3	$0.35^{+0.04}_{-0.04}$
NGC 5098	LE	186.0 ± 4.8	0.214	…	$0.96^{+0.61+}_{-0.22}$	$4.47^{+0.51}_{-0.53}$	183.9	$0.09^{+0.01}_{-0.01}$
A3571	NLE	253.1 ± 4.9	0.396	…	$9.80^{+1.88}_{-1.54}$	$56.54^{+6.90}_{-5.57}$	559.7	$2.59^{+0.21}_{-0.20}$
A1991	LE	221.7 ± 8.0	0.304	0.44	$1.64^{+0.12}_{-0.07}$	$17.89^{+0.12}_{-0.08}$	331.9	$0.55^{+0.01}_{-0.01}$
A2107	NLE	246.7 ± 5.1	0.377	…	$4.00^{+0.66}_{-0.65}$	$27.72^{+1.95}_{-1.82}$	413.9	$1.05^{+0.05}_{-0.06}$
Region F								
MS 0735+7421	LE	314.5 ± 17.4	0.612	…	$7.25^{+0.06}_{-0.30}$	$96.28^{+0.57}_{-2.65}$	507.7	$2.31^{+0.08}_{-0.08}$
A665	NLE	362.8 ± 7.0^c	0.810	…	$9.47^{+3.11}_{-1.95}$	$95.62^{+23.02}_{-15.59}$	501.9	$2.15^{+0.23}_{-0.25}$
4C+55.16	LE	274.0 ± 24.1	0.464	…	$2.06^{+0.72}_{-0.39}$	$47.52^{+9.84}_{-6.27}$	455.2	$1.71^{+0.19}_{-0.17}$
Zw2701	LE	340.8 ± 17.3	0.718	…	$1.37^{+0.23}_{-0.22}$	$41.21^{+2.37}_{-2.58}$	466.6	$1.79^{+0.08}_{-0.09}$
A1689	NLE	355.3 ± 17.7	0.781	…	$2.44^{+0.61}_{-0.06}$	$102.73^{+7.95}_{-1.03}$	718.2	$6.31^{+0.18}_{-0.34}$

Table 2
(Continued)

Cluster	Lines?	σ_* (km s^{-1})	$\rho_{0,\mathrm{ISO}}$ (keV)	Beta	$R_{s,\mathrm{NFW}}$ (arcmin)	$\rho_{0,\mathrm{NFW}}$ (keV)	R_{2500} (kpc)	M_{2500} ($\times 10^{14}\,M_\odot$)
A1758[a]	NLE	376.5 ± 21.0	0.01(0.877)	0.81	$1.22^{+0.53}_{-0.32}$	$17.56^{+4.83}_{-3.39}$	251.7	$0.30^{+0.04}_{-0.04}$
MACS 1347−11	LE	362.8 ± 7.0^{c}	0.810	$\cdots$	$1.06^{+0.20}_{-0.08}$	$163.23^{+12.17}_{-5.25}$	776.3	$10.77^{+0.07}_{-0.07}$
A1835	LE	485.6 ± 24.2	1.458	$\cdots$	$5.46^{+0.51}_{-0.78}$	$143.91^{+11.17}_{-16.71}$	711.3	$6.61^{+0.37}_{-0.38}$
MACS 1423+24	LE	362.8 ± 7.0^{c}	0.810	$\cdots$	$0.96^{+0.33}_{-0.10}$	$74.93^{+11.86}_{-5.67}$	501.8	$3.24^{+0.03}_{-0.03}$
Zw7160	LE	428.1 ± 20.5	1.134	$\cdots$	$1.44^{+0.23}_{-0.15}$	$47.28^{+3.49}_{-2.82}$	497.8	$2.28^{+0.11}_{-0.11}$
MACS 1532+30	LE	362.8 ± 7.0^{c}	0.810	$\cdots$	$1.90^{+0.38}_{-0.24}$	$81.95^{+10.80}_{-5.82}$	570.1	$3.76^{+0.32}_{-0.32}$
A2219	NLE	342.5 ± 21.9	0.726	$\cdots$	$4.52^{+0.51}_{-0.48}$	$120.63^{+8.78}_{-8.78}$	678.8	$5.57^{+0.23}_{-0.23}$
A2390	LE	348.2 ± 22.5	0.750	$\cdots$	$4.68^{+0.70}_{-0.74}$	$118.75^{+13.15}_{-13.09}$	664.3	$5.24^{+0.37}_{-0.34}$
Region G								
RX J0338+09	LE	215.4 ± 4.8	0.287	$\cdots$	$4.98^{+0.38}_{-0.17}$	$29.12^{+1.08}_{-0.36}$	418.9	$1.08^{+0.03}_{-0.04}$
A496	LE	228.1 ± 4.6	0.320	$\cdots$	$14.00^{+2.88}_{-2.09}$	$45.65^{+5.93}_{-3.68}$	482.5	$1.65^{+0.11}_{-0.11}$
A2052	LE	221.1 ± 5.4	0.302	0.62	$5.55^{+0.17}_{-0.27}$	$25.65^{+0.15}_{-0.06}$	394.2	$0.90^{+0.09}_{-0.09}$
A2199	LE	238.9 ± 4.0	0.351	$\cdots$	$26.05^{+2.41}_{-3.07}$	$72.48^{+5.43}_{-6.82}$	558.1	$2.54^{+0.12}_{-0.18}$
IC1262	LE	184.7 ± 4.8	0.211	$\cdots$	$3.04^{+0.25}_{-0.24}$	$12.52^{+0.28}_{-0.36}$	283.0	$0.33^{+0.01}_{-0.01}$

Notes. Columns are: (i) cluster name, (ii) line-emitting (LE) or non-line-emitting (NLE) BCG, indicative of cool-core, (iii) equivalent stellar velocity dispersion, (iv) isothermal potential $= \mu m_H \sigma^2$ where m_H is the mass of the hydrogen atom and the mean atomic weight $\mu = 0.59$, (v) NFW scale radius, (vi) NFW potential $= 4\pi G \rho_0 R_s^2 \mu M_H$ in units of keV, (vii) R_{2500}, (viii) M_{2500}. The reported $\rho_{0,\mathrm{ISO}}$ values correspond to the σ_* values and were kept fixed in the fitting to account for the anchored stellar mass component. Sources are ordered as in Table 1. A β-model was used to account for cluster emission outside of the outermost annulus in instances where there was still clearly cluster X-ray emission beyond this. Errors on M_{2500} do not include the additional 5% systematic uncertainty. See the text for more details.
[a] No clear BCG (and cluster appears to be highly out of equilibrium); mass estimates accordingly less certain. Given *isopot* value are for closest bright galaxy to cluster center but a minimal isothermal component is used during fitting.
[b] Potentially heightened BCG luminosity/equivalent stellar dispersion due to possible ongoing merger.
[c] Denotes a 2MASS drop-out.
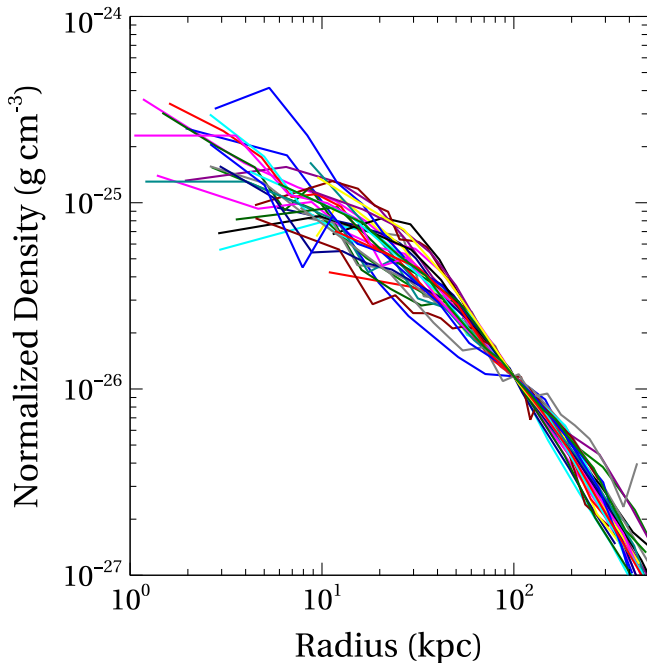
Figure 3. Deprojected density ρ profiles (see also Figure 2) normalized to median density at 100 kpc for the Hα-emitting clusters in our sample. Density is plotted in mass units for ease of comparison with other studies. Profiles have been randomly assigned colors for presentation purposes.

The central atmospheric gas density is correlated with molecular gas mass, indicating the molecular gas likely condensed from the hot atmospheres (Paper II).

5.2. Cluster Entropy Profiles

The shape of the central entropy profiles in cool cores is key to understanding thermally unstable cooling (Sharma et al. 2012; Voit et al. 2017). For example, in systems where heat is injected centrally, the atmosphere of the core may be almost isentropic (Voit et al. 2017). Beyond the core, convection may stabilize gas against thermal instability, unless low-entropy gas is uplifted allowing it to cool (McNamara et al. 2016).

Gravitational infall imprints an entropy power law of the form $K \propto r^{1.1}$ (e.g., Tozzi & Norman 2001; Voit et al. 2005). Other, non-gravitational processes, such as AGN outbursts, may enhance the inner entropy, flattening the profile. Early *Chandra* observations indeed found flat or flattening inner entropy profiles in clusters (e.g., David et al. 1996, 2001; Ponman et al. 1999, 2003) which may be fitted functionally as $K(r) = K_0 + K_{100}(r/100\,\mathrm{kpc})^\alpha$ (Donahue et al. 2005, 2006; Cavagnolo et al. 2008, 2009; Voit et al. 2017). This form provides a good approximation to clusters with high central entropy (Cavagnolo et al. 2009). However, it poorly represents cool cores. Panagoulia et al. (2014) found that cool cores are instead characterized by broken power laws. The inner 50 kpc are well described by a $K \propto r^{0.67}$ scaling that persists down to at least a few kpc. Similarly both Lakhchaura et al. (2016) and Hogan et al. (2017) found cool-core entropy profiles continuing to fall down to small radii.

In Figure 4 we present fully deprojected entropy profiles for the 33 clusters with central Hα emission, 14 of which overlap with Panagoulia et al.'s (2014) sample. We have overlain Panagoulia et al.'s (2014) mean profile of $K = 95.4 \times (r/100\,\mathrm{kpc})^{0.67}$ and it
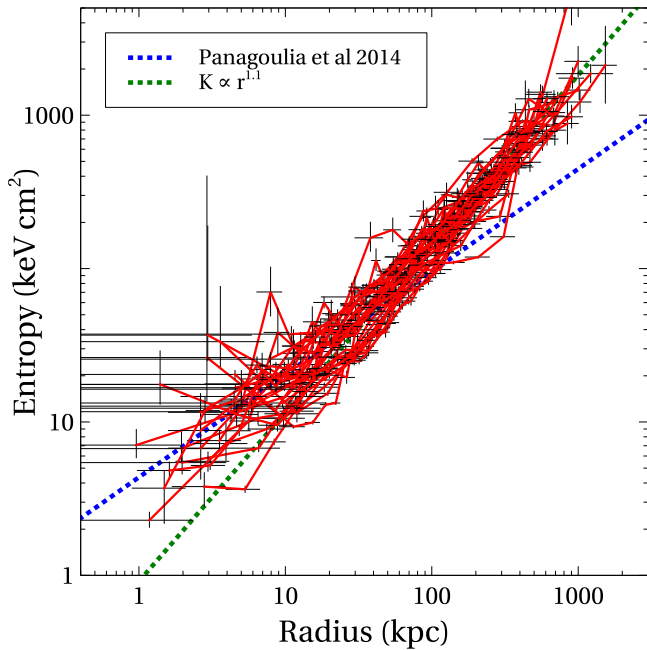
Figure 4. Entropy profiles of all clusters in our sample that display Hα emission. Our inner profiles are in agreement with the average fitted entropy profile of Panagoulia et al. (2014). At larger radii we find good agreement with the standard entropy profile power-law shape expected from gravity alone (Tozzi & Norman 2001; Voit et al. 2005). The dashed green line shown here is taken as a representative cluster; see the text.

Figure 5. Difference between our calculated entropy profiles and the best-fit profile from Panagoulia et al. (2014), as a function of radius, for clusters in Figure 4. An isentropic core would cause points to lie systematically above the zero-point. At large radii (∼50 kpc) there is a systematic steepening of the entropy profiles. The connecting lines for individual clusters have been removed since we are interested in the overall trend here.

agrees with ours. At large radii the profiles steepen to match the baseline $K \propto r^{1.1}$ power-law scaling expected from gravity alone (e.g., Tozzi & Norman 2001; Voit et al. 2005). The self-similar entropy profile derived by Voit et al. (2005) takes the form $K = 1.32 \times K_{200}(r/R_{200})^{1.1}$, where K_{200} is the entropy at R_{200}. Our individual mass profiles become increasingly uncertain beyond R_{2500} (Hogan et al. 2017). To obtain an approximate K_{200} for our sample we take the calculated $R_{200} \approx 1240$ kpc for a fiducial rich cluster from Voit et al. (2005), and extrapolate our entropy profile distributions to this radius. This gives $K_{200} \approx 1750$ keV cm^2, which is the normalization plotted in Figure 4.

In Figure 5 we plot the difference between our calculated entropy profiles and the best-fit profile of Panagoulia et al. (2014) as a function of radius. The profiles agree below ∼50 kpc, down to ∼1 kpc, whereas large isentropic cores, if they existed, would raise the points systematically above the zero-point at low radii. We do find such a rise above 50 kpc, consistent with the index steepening to $K \propto r^{1.1}$ as seen in Figure 4.

Further flattening of the entropy profiles is likely on smaller scales than probed here (see e.g., Donahue et al. 2006), especially once the acceleration associated with the central SMBH becomes more relevant. However, we find that down to a resolution limit of ∼1 kpc the entropy profiles of our cool-core clusters are consistent with a broken power law.

6. The Onset of Gas Condensation

The mass profiles derived in Section 4.2 were used to calculate t_{ff} profiles for each cluster. A 10% systematic error on mass was assumed and propagated into t_{ff} (see, Hogan et al. 2017). Combining these with the atmospheric modeling from Section 4.1 we present projected and deprojected profiles for

both t_{cool} and t_{cool}/t_{ff} (Figures 6 and 7 respectively). We indicate in the left-hand panels of Figures 6 and 7 the approximate thresholds of 5×10^8 and 1.0×10^9 years, below which nebular emission and star formation are observed (Cavagnolo et al. 2008; Rafferty et al. 2008). In the right-hand panels of these figures we indicate t_{cool}/t_{ff} threshold values of 10 and 20.

Comparison of the left-hand panels of Figures 6 and 7 shows that once projection effects are accounted for, we recover the bimodality between clusters with short and long cooling times. Abell 2029, with its short $t_{c,central}$ yet no Hα emission (McDonald et al. 2010) is clearly an outlier (discussed extensively in McNamara et al. 2016). The right-hand panels similarly split between LE and NLE clusters, A2029 again being an outlier. The values of $(t_{cool}/t_{ff})_{min}$ for objects with central Hα emission (red lines) range between 8.8 and 30.3, with a mean of 16.5 and standard deviation of 5.7. Only a single cluster lies below $t_{cool}/t_{ff} = 10$, but not significantly so (within 1σ). Therefore, deviations below 10 do not occur or are extremely rare (see also Paper II).

The radially averaged profiles do not capture the full range of t_{cool}/t_{ff} that may exist at each altitude. Cooler inclusions of gas with shorter than average cooling times mixed into the atmosphere will have smaller than average t_{cool}/t_{ff} that fall below 10. Our measurements exclude models where linear density perturbations grow thermally unstable when $t_{cool}/t_{ff} < 10$.

With A2029 included (excluded), the non-line-emitters (black lines) have $(t_{cool}/t_{ff})_{min}$ spanning 17.8 (30.8)–101.4, with a mean of 62.8 (60.8) and standard deviation of 22.8 (21.4). Error bars have been excluded on Figures 6 and 7 for clarity. However, the right-hand panel of Figure 7 suggests that the location of the t_{cool}/t_{ff} minimum is noisy. Figure 8 shows a histogram of the number of annuli at radii below that in which the minimum t_{cool}/t_{ff} is measured, for all 33 Hα-emitting

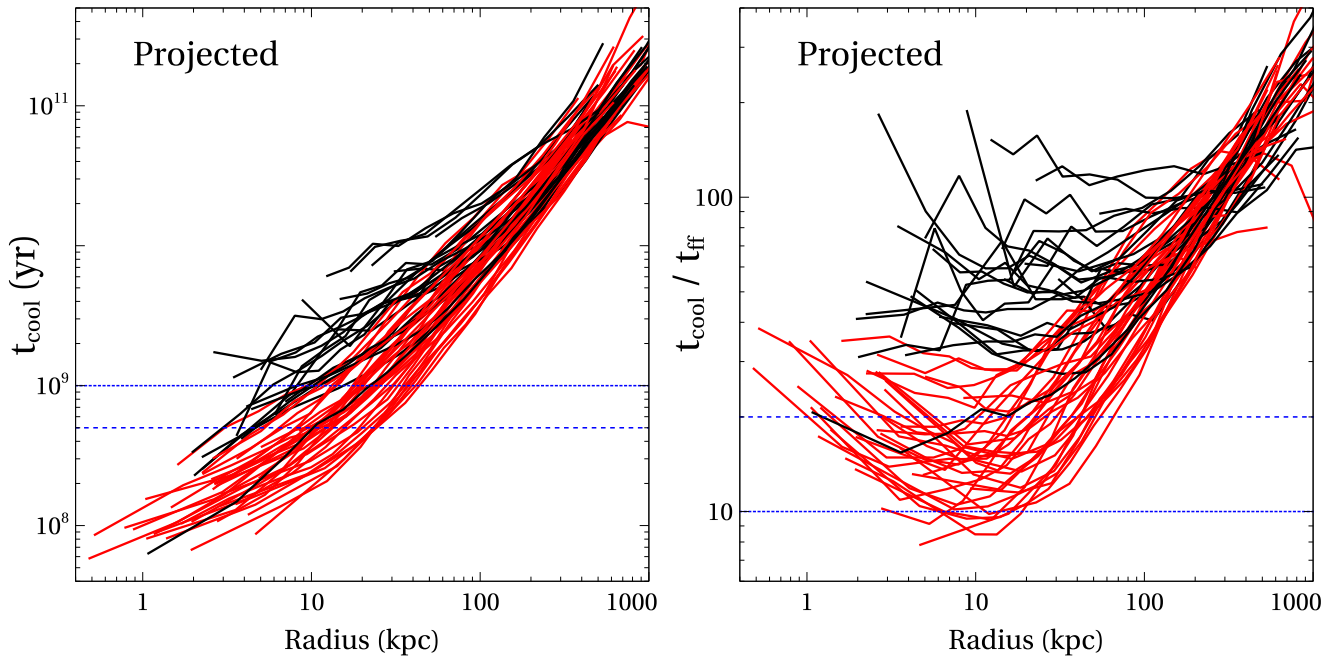**Figure 6.** Projected cooling time (left) and t_{cool}/t_{ff} (right), colorized by the presence (red) or absence (black) of nebular emission. Clusters lacking nebular emission indicative of ongoing gas condensation typically have both higher central t_{cool} and t_{cool}/t_{ff}. Most of the black profiles apparently violating the $t_{cool} < 1$ Gyr threshold do so only due to projection effects (see Figure 7). The single cluster without nebular emission yet with a central cooling time below 1×10^8 years and a $(t_{cool}/t_{ff})_{min} < 20$ is A2029. Error bars are omitted for clarity.

clusters. This implies that $R(t_{cool}/t_{ff})_{min}$ values are usually poorly resolved (in all studies thus far), and so are unreliable (see also Section 7).

6.1. Thresholds in t_{cool} and t_{cool}/t_{ff}

The range in both t_{cool} and t_{cool}/t_{ff} are shown in Figure 9. The sharp threshold for the onset of nebular emission is evident. Hα luminosity is plotted here against deprojected values of t_{cool}, the minimum of t_{cool}/t_{ff}, and t_{cool} rescaled to lie in a similar range to $(t_{cool}/t_{ff})_{min}$. These quantities are measured both at $R(t_{cool}/t_{ff})_{min}$ (top panels, Figure 9) and at a radius of 10 kpc (bottom panels, Figure 9). The Hα luminosities were measured heterogeneously and taken from Crawford et al. (1999), Cavagnolo et al. (2009), McDonald et al. (2010), and Rawle et al. (2012). Therefore the absolute value of the Hα luminosity is uncertain, but the detection of nebular emission indicates cold gas. A radius of 10 kpc was chosen to ensure most objects are resolved or require only a short extrapolation. Thermodynamic parameters could instead be presented at a fixed scale radius. We investigated this by measuring each parameter shown in Figure 9 at $R/R_{2500} = 0.02$. The results were essentially equivalent to those at 10 kpc. Our conclusions are therefore not affected by whether we choose to use a fixed physical radius of 10 kpc or fixed scaled radius of 0.02 R_{2500}. Similar distributions in these parameters are found in Paper II, using CO observations as a cooling indicator in place of Hα.

Inspection of Figure 9 shows that the threshold between the Hα emitters and non-emitters is equally sharp for t_{cool} alone or t_{cool}/t_{ff} (left-hand or middle panels respectively). However, we have added a variable (t_{ff}) which immediately indicates that the threshold is driven by cooling time. That only a single cooling cluster lies below $(t_{cool}/t_{ff})_{min} = 10$ is noteworthy, and in this instance it lies below by less than one standard deviation and is thus insignificant. Similarly, we find in Paper II that only one of

55 clusters harboring molecular gas reservoirs lies below $t_{cool}/t_{ff} = 10$, and this once again is statistically insignificant.

The absence of clusters lying below $t_{cool}/t_{ff} = 10$ is problematic for thermally unstable cooling models positing that linear density perturbations grow to become thermally unstable when $t_{cool}/t_{ff} < 10$ (e.g., McCourt et al. 2012; Sharma et al. 2012; Prasad et al. 2015; Choudhury & Sharma 2016). In Figure 10 we plot the cooling time profiles for the Hα-emitting sources in our sample. We find a small range in central cooling time, and this range is reduced further when normalized to R_{2500}. This reflects the small spread in densities found in Section 5.1. Furthermore, we find no correlation between the central cooling time and either cavity power or the radio luminosity of the central AGN. These results, as in Section 5.1, show that atmospheres do not respond dramatically to powerful AGN activity.

Li et al. (2015) simulated a precipitating, self-regulating cool-core cluster that ran for ~6.5 Gyr. They found that t_{cool}/t_{ff} falls below 10 and approaches unity in the most thermally unstable cooling phase roughly 25%–30% of the time. Could we have missed those systems passing through their most rapid cooling phase? To answer this question we adopt 1×10^{43} erg s^{-1} as the average cavity power required to offset cooling (Rafferty et al. 2006). Converting to an equivalent 1.4 GHz radio-luminosity of ~7×10^{24} W Hz^{-1} following Bîrzan et al. (2004), and using the radio luminosity functions presented in Hogan et al. (2015b), we find approximately 20%–30% of BCGs host a radio-AGN $\gtrsim 7 \times 10^{24}$ W Hz^{-1}. Equating these periods when the AGN launches powerful jets as the period during which feedback is "on," hence when we expect ongoing fuelling of the AGN, then this fraction agrees with the fraction of time with $t_{cool}/t_{ff} < 10$ in Li et al. (2015). If thermally unstable cooling occurs when $t_{cool}/t_{ff} < 10$, ~25% of our sample, or roughly 22 clusters from the combined
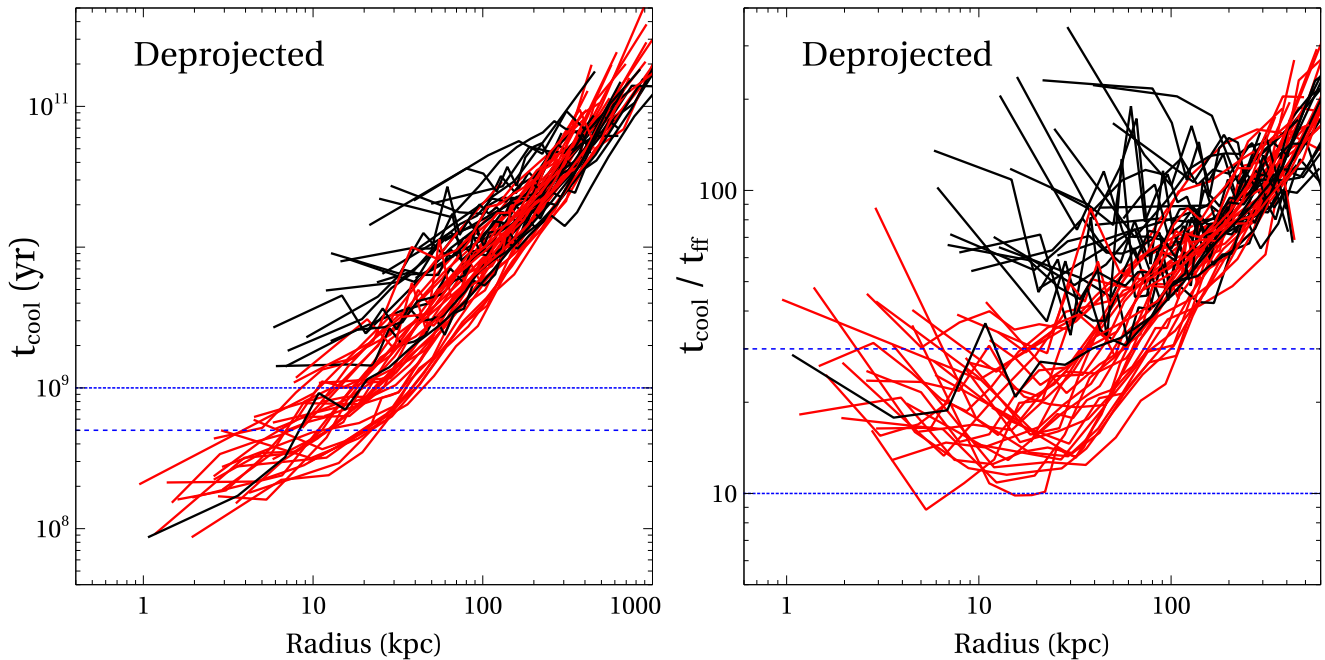
Figure 7. Deprojected version of Figure 7. Note that several clusters, mainly the more diffuse systems, had too few counts in their central annuli for successful fitting after deprojection and so these profiles sometimes truncate at larger radii than their projected analogues. The cooling threshold in the left panel is more sharply defined than in Figure 6, with only the well-known outlier A2029 having $t_{cool} < 1$ Gyr at 10 kpc among the non-nebular clusters. Most cooling clusters have $(t_{cool}/t_{ff})_{min}$ in the range 10–30. Error bars are omitted for clarity.
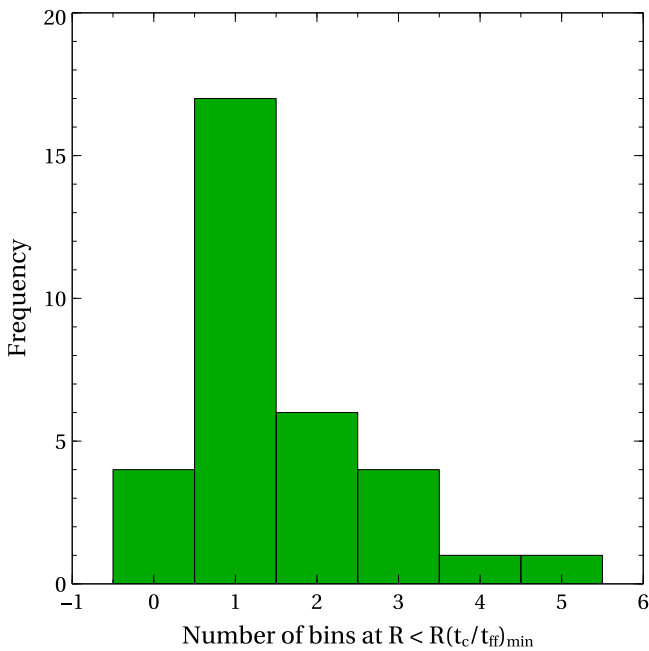
Figure 8. Histogram showing the number of annuli within the annulus having the minimum deprojected t_{cool}/t_{ff} (see Figure 7) for the 33 Hα-emitting clusters in the sample. In most cases, there is only a single (noisy) bin at smaller radii, showing that the minima are not well resolved.

samples here and from Pulido et al. should lie below this threshold. Yet no object falls significantly below 10.

6.2. Ratio Driven by Cooling Time

McNamara et al. (2016) pointed out that the free-fall times found in other studies at the radius of $(t_{cool}/t_{ff})_{min}$ span a narrow range. As a consequence, they showed that the t_{cool}/t_{ff} threshold is driven almost entirely by t_{cool}. In Figure 11 we plot

the distributions of free-fall and cooling times of our sample clusters taken at a radius of 10 kpc. Among the full sample (left-hand panel) we find a wider spread in cooling time than free-fall time. The difference in range declines for LE clusters (right-hand panel, Figure 11). The ratio of the standard deviation to the mean is roughly 6 times higher for the distribution of cooling times than the free-fall times. When only Hα emitters are considered this factor falls to 2.5. Dividing t_{cool} by t_{ff} is akin to dividing by a constant with a small variance. Thus the numerator drives the ratio. It is therefore difficult to understand the role of t_{ff} in thermal instability.

In the left-hand panel of Figure 12 we plot both t_{cool} and t_{ff} at the location of $R(t_{cool}/t_{ff})_{min}$, as a function of $(t_{cool}/t_{ff})_{min}$. Among the full sample we find that both t_{cool} and t_{ff} are correlated with the ratio, with Kendalls tau values of 0.71 and 0.56 (both P-value $<1 \times 10^{-6}$) respectively. However, the gas in the non-cool-core systems is expected to be thermally stable (both t_{cool} and t_{cool}/t_{ff} lie well above unity) and are largely irrelevant to the argument. They may also suffer resolution bias in their $(t_{cool}/t_{ff})_{min}$ due to the relatively large truncation radii of their cooling profiles. Considering only the Hα-emitting sub-sample we find t_{cool} to be much more dominant in driving the ratio (Kendalls tau = 0.48, P-value 1.2×104) than t_{ff} (Kendalls tau = 0.21, P-value 0.1). The inclusion of t_{ff} does not improve the predictive power for the onset of gas cooling above that of the cooling time alone (Section 6.1, see also McNamara et al. 2016).

6.2.1. A Selection Effect Explains the Narrow Range in $(t_{cool}/t_{ff})_{min}$

We show here that the narrow range in minimum t_{cool}/t_{ff} is a consequence of the correlation between cooling time, free-fall time, and radius, and the noise imprinted by resolution effects on the measured radius of t_{cool}/t_{ff} minimum. Comparing the spread in L(Hα) plotted against t_{cool} alone (left-hand panel, Figure 9) and t_{cool}/t_{ff} (middle panel, Figure 9) may be

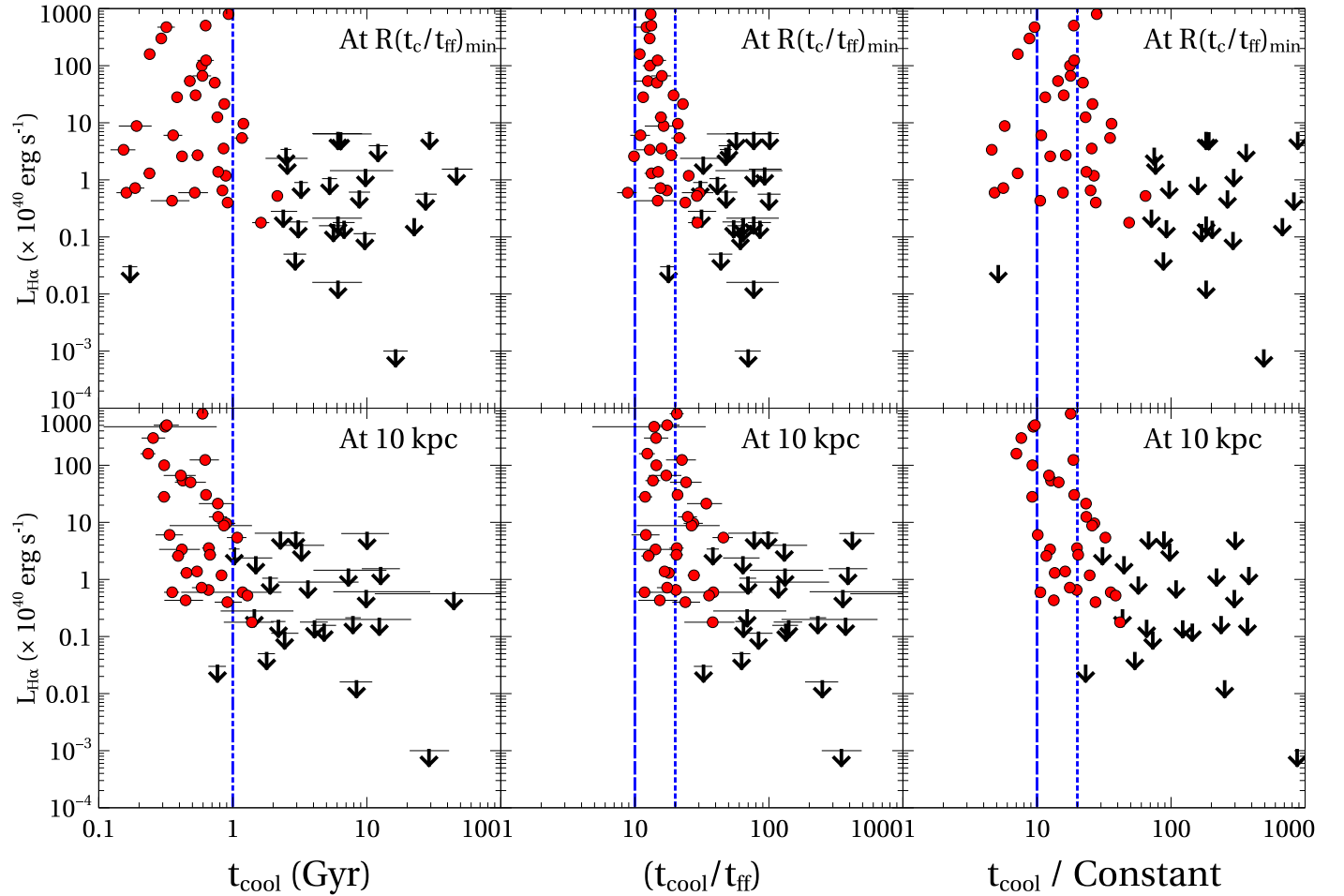**Figure 9.** Hα luminosity of the central galaxy as a function of the deprojected cooling time (left), $(t_{\rm cool}/t_{\rm ff})_{\rm min}$ (middle), and the cooling time rescaled to lie in a similar range to $(t_{\rm cool}/t_{\rm ff})_{\rm min}$ (right). The top panels measure each of these quantities at the radius where $(t_{\rm cool}/t_{\rm ff})_{\rm min}$ is recorded, $R(t_{\rm cool}/t_{\rm ff})_{\rm min}$, whereas the bottom panels show the equivalent quantities taken at a constant radius of 10 kpc. We note three results. First, the onset of cooling appears no sharper in $t_{\rm cool}/t_{\rm ff}$ than in $t_{\rm cool}$ alone. Second, no clusters have $(t_{\rm cool}/t_{\rm ff})_{\rm min}$ significantly below 10, in tension with predictions. Third, the range in $(t_{\rm cool}/t_{\rm ff})_{\rm min}$ is narrower than the equivalent range in $t_{\rm cool}$ when both are measured at the location of the $t_{\rm cool}/t_{\rm ff}$ minimum, though the effect is reduced when measured at a single radius. This narrowing of the range is initially perplexing since there is very little spread in $t_{\rm ff}$ (see Section 6.2). We find the same results if a fixed scale radius of $R/R_{2500} = 0.02$ is used in place of a fixed physical radius of 10 kpc.

misleading because of the logarithmic scaling. We therefore consider instead the standard deviation (σ) in the $(t_{\rm cool}/t_{\rm ff})_{\rm min}$ of the Hα emitters compared to $t_{\rm cool}$ normalized by its mean value, $t_{\rm cool}/\langle t_{\rm cool}\rangle$.

When measured at $R(t_{\rm cool}/t_{\rm ff})_{\rm min}$ we recover a narrower spread in $t_{\rm cool}/t_{\rm ff}$ ($\sigma = 0.34$) than $t_{\rm cool}/\langle t_{\rm cool}\rangle$ ($\sigma = 0.65$), suggesting that dividing by $t_{\rm ff}$ tightens the range. However, because $t_{\rm ff} = R/\sigma$ (see Section 7), and considering the narrow range of σ, $R(t_{\rm cool}/t_{\rm ff})_{\rm min}$ is strongly correlated with $t_{\rm cool}$. We are thus condemned to measure $(t_{\rm cool}/t_{\rm ff})_{\rm min}$ over a narrower range than $t_{\rm cool}$ alone at $R(t_{\rm cool}/t_{\rm ff})_{\rm min}$. For example, a measurement of the spread in $(t_{\rm cool}/t_{\rm ff})_{\rm min}$ versus the spread in $t_{\rm cool}$ at a fixed radius reveals $\sigma = 0.43$ for $t_{\rm cool}/\langle t_{\rm cool}\rangle$ at 10 kpc, which is much narrower than the spread measured at $R(t_{\rm cool}/t_{\rm ff})_{\rm min}$. Adding to this model-dependent effect is a general bias that the distribution of the minimum of a number of samples of a random variable is narrower than the distribution of the underlying random variable. Indeed, if we instead take $t_{\rm cool}/t_{\rm ff}$ at a fixed physical radius of 10 kpc, the spread in $t_{\rm cool}/t_{\rm ff}$ ($\sigma = 0.50$) is comparable to that in $t_{\rm cool}/\langle t_{\rm cool}\rangle$.

This systematic effect is shown clearly in the left-hand panel of Figure 12. The points there are color-coded by $R(t_{\rm cool}/t_{\rm ff})_{\rm min}$.

A matching vertical color-gradient is seen in both $t_{\rm cool}$ and $t_{\rm ff}$ for any constant value of $(t_{\rm cool}/t_{\rm ff})_{\rm min}$. This shows that for a given value of $(t_{\rm cool}/t_{\rm ff})_{\rm min}$ the ratio $t_{\rm cool}/t_{\rm ff}$ is determined by the radius at which it is measured and thus this ratio must lie in a narrow range: when $t_{\rm cool}$ is large, $t_{\rm ff}$ is large, and conversely so. In the right-hand panel of Figure 12 we plot $t_{\rm cool}$ versus $t_{\rm ff}$ at $R(t_{\rm cool}/t_{\rm ff})_{\rm min}$ (the numerator against the denominator). The sharp lower bound at $(t_{\rm cool}/t_{\rm ff})_{\rm min} = 10$ is a consequence of the lowest measured values of the cooling time and the lowest values of the free-fall time shown in Figure 11 differing by a factor of 10. Adding to this the noise in the estimate of $R(t_{\rm cool}/t_{\rm ff})_{\rm min}$ (Figures 7 and 8) and we have the elements of a systematic bias. We cannot exclude out of hand that the apparent floor in $(t_{\rm cool}/t_{\rm ff})_{\rm min}$ is a natural consequence of feedback (e.g., Voit et al. 2015). However, a physical floor cannot be disentangled from a systematic bias. Furthermore, comparisons between $R(t_{\rm cool}/t_{\rm ff})_{\rm min}$ with other thermodynamic properties of interest have failed to reveal correlations (Paper II). The only way to disentangle this bias from a physical correlation would be to identify a sample of galaxies with a broader range of mass (i.e., vary the denominator), which would be difficult.
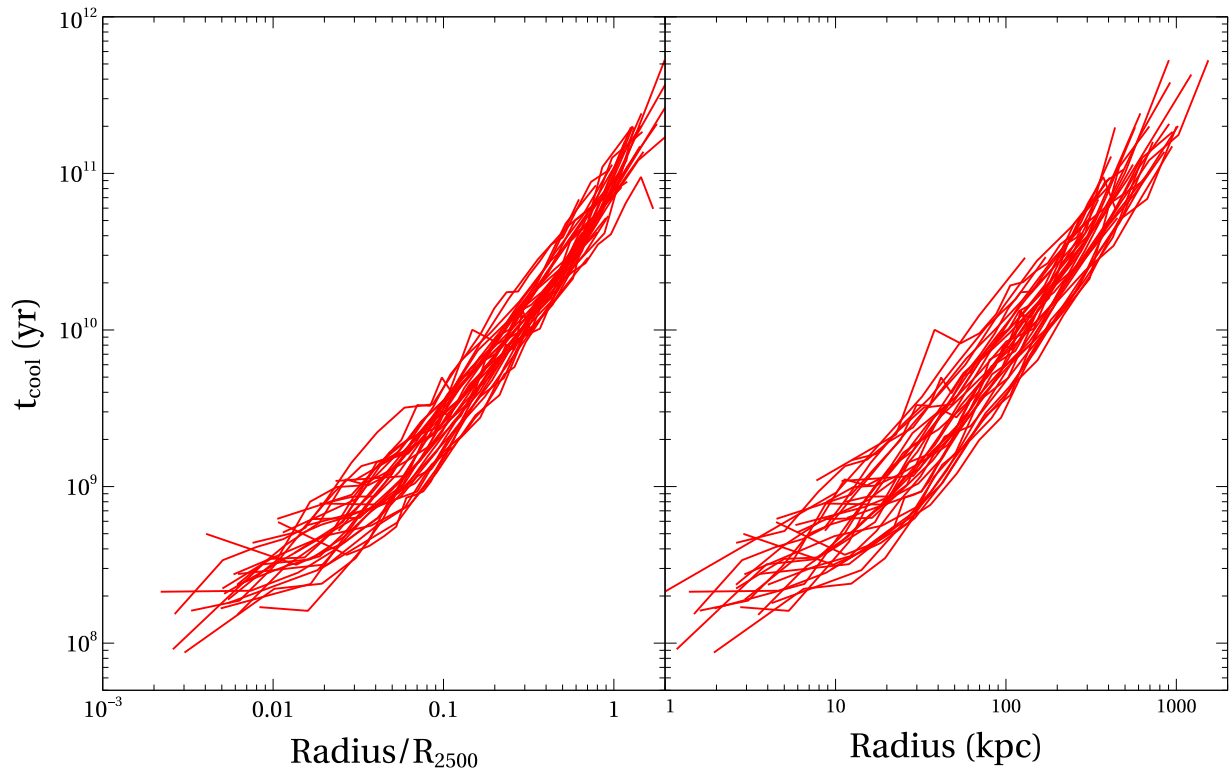
Figure 10. Cooling time profiles for the LE clusters in our sample. In the left-hand panel the radius is normalized by the R_{2500} whereas in the right-hand panel physical radius is plotted. Rescaling the radius reduces the scatter at both large and small radii.

7. A Floor Rather than a Minimum in t_{cool}/t_{ff}

Here we consider the possibility that the minimum in the t_{cool}/t_{ff} profiles may actually be a floor, rather than a clear minimum. This possibility arises naturally when the mass profile is approximately isothermal within the minimum t_{cool}/t_{ff} and when the entropy profile follows a power-law slope of $K \propto r^{2/3}$ within this region (see Section 5.2, also Panagoulia et al. 2014). We find that both conditions are met in our sample (Panagoulia et al. 2014; Hogan et al. 2017, and Figure 4 here), and likely in general (e.g., Koopmans et al. 2009).

We observe an inner entropy index $K = Ar^{2/3}$ where A is a constant. From Section 4.1.1 we have that $n_e = (kT/K)^{3/2}$ and $t_{cool} \propto P/(n_e^2 \Lambda)$, where the cooling function Λ depends only on abundance and temperature. Substituting for pressure and density leads to $t_{cool} \propto K^{3/2}/((kT)^{1/2}\Lambda) \propto (A^{3/2}r)/((kT)^{1/2}\Lambda)$. Using Equation (3) and the mass distribution for an isothermal sphere, $M = (2\sigma^2 r)/G$, gives $t_{ff} = r/\sigma$. Combining these we end up with the radial dependences cancelling to give $(t_{cool}/t_{ff}) \propto \Sigma/(\Lambda(kT)^{(1/2)})$. This expression has no dependence on radius, implying that t_{cool}/t_{ff} should decline to a constant at a finite radius. We expect then that the upturns at small radii seen for example in Figures 6 and 7 and in all other studies are produced by the increasing impact of density inhomogeneities along the line of sight at small radii.

7.1. Potential Low-altitude Systematic Effects

Systematic errors induced by limited resolution at small radii in either, or both, the numerator or denominator of t_{cool}/t_{ff} could introduce noise and artifically flatten the profile. For example, overestimating the inner mass would underestimate t_{ff}. However, we have attempted to buttress ourselves against this. Note that our $(t_{cool}/t_{ff})_{min}$ are found around 10 kpc. Hogan

et al. (2017) derived mass profiles that matched those inferred from stellar velocity dispersions (Fisher et al. 1995) down to $\sim$1 kpc. Furthermore, Figure 11 shows that t_{cool} drives the t_{cool}/t_{ff} ratio (also see Section 6). We expect most systematics in the inner shape of the profiles concern the measurement of t_{cool}.

The t_{cool} measured in a central annulus (usually with $r_{inner} = 0$) may be overestimated by high-temperature gas projected from higher altitudes (Hogan et al. 2017). A more subtle effect concerns the common assumption that t_{cool} is approximately constant within a radial shell when creating cooling profiles assuming radial symmetry. At higher altitudes this assumption is reasonable since the clusters are largely smooth and any structure is averaged over a large volume. However, almost all cool-core clusters contain cavities in their central atmospheres and the assumption of spherical symmetry breaks down at small radii. Single-temperature model fits represent the hot gas from which cold gas originates. Inhomogeneities in the hot atmospheres associated with dense gas are prevalent at smaller radii. While we attempted to excise bright, lumpy structure from our analysis, it is nearly impossible to do so completely toward the cluster center. Therefore a systematic effect may remain where the measured average t_{cool} is lower at small radii compared to the undisturbed atmosphere. A spread in t_{cool}/t_{ff} values is expected, especially at small radii. The values of t_{cool} (or t_{cool}/t_{ff}) are likely to vary so that sites of rapid cooling are likely to occur where t_{cool} reaches a minimum (also see the discussion in Meece et al. 2015).

Of the 33 LE clusters in our sample, $(t_{cool}/t_{ff})_{min}$ is found in the innermost annulus of four (see Figure 8), which are clearly unresolved. Seventeen others have only a single spatial bin lying below the position of $R(t_{cool}/t_{ff})_{min}$ and a further six have
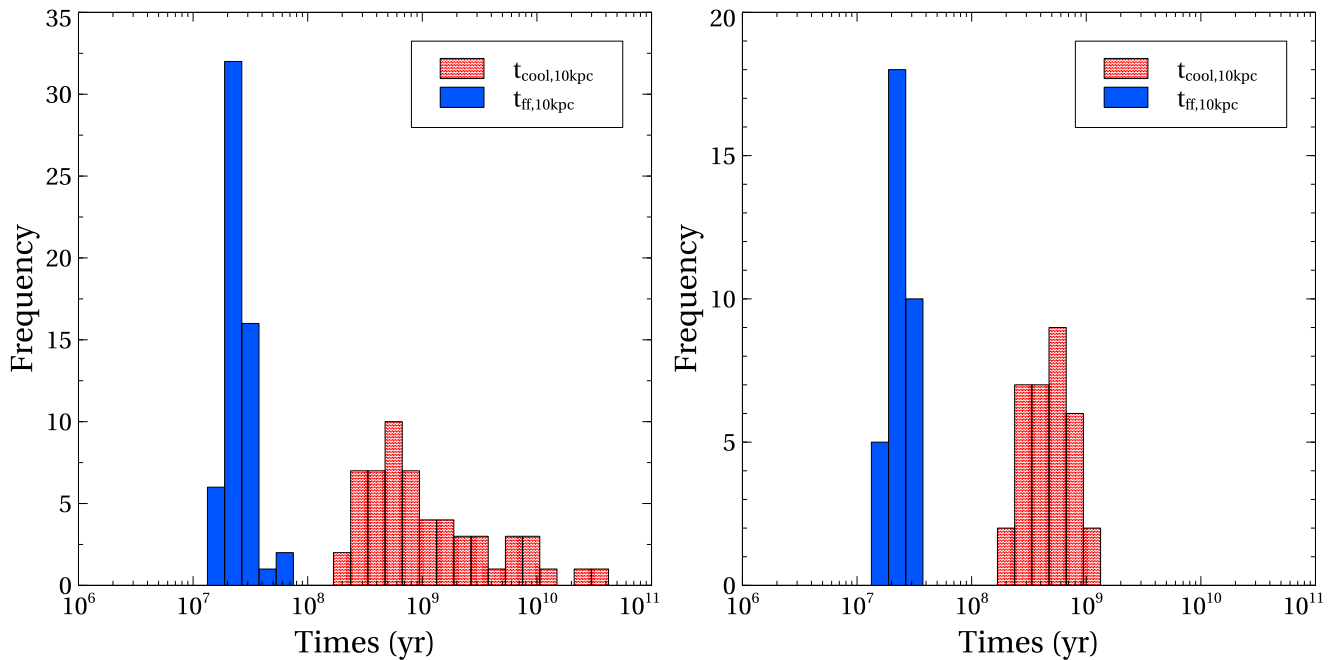
Figure 11. Spread of cooling and free-fall times at 10 kpc. The left-hand panel shows the full sample whereas the right-hand panel is restricted only to the 33 sources that are known to exhibit Hα emission. Among the full sample it is clear that the range in cooling time is much wider than, and therefore dominant over, that of the free-fall time. When restricted to only the LE clusters the effect is lessened but nevertheless still apparent.

only two bins below the minimum. The 17 are, likewise, unresolved and the six with two bins are marginally resolved. Among the six, the value of $t_{\rm cool}/t_{\rm ff}$ in the adjacent annulus within $R(t_{\rm cool}/t_{\rm ff})_{\rm min}$ is $<1\sigma$ greater than the minimum in each case. To investigate this further, we calculated the equivalent cooling time profiles $t_{\rm c,eq}$ that would lead to a flat $t_{\rm cool}/t_{\rm ff}$ profile below the $R(t_{\rm cool}/t_{\rm ff})_{\rm min}$ for each of our clusters (i.e., $t_{\rm c,eq} = (t_{\rm c}/t_{\rm ff})_{\rm min} \times t_{\rm ff}$). We found that the original $t_{\rm cool}$ profiles are consistent to within one standard deviation of $t_{\rm cool}/t_{\rm ff}$, being flat for 27 of 33 instances. The inner atmospheres of the remaining six clusters (A478, MS 0735+7421, PKS 0745−191, Zw2701, Hercules A, and Zw8276) are inhomogeneous, and thus indeterminate. It is at least plausible that rises observed below the minima seen here and in other studies are artificial, and that inner $t_{\rm cool}/t_{\rm ff}$ profiles are instead flat. A measurement bias may have previously masked these flat profiles. Regardless of whether the inner profile is truly flat or not, the minimum value is always lower than any other. This can create the misleading impression that the inner profile turns upward inside the minimum, particularly when there are few data points at smaller radii.

Among this sample the region inside $R(t_{\rm cool}/t_{\rm ff})_{\rm min}$ is best resolved for Hydra A. Notably, its $t_{\rm cool}/t_{\rm ff}$ profile flattens at its center (Figure 13). This is perhaps surprising considering the expected systematic bias from a heavily structured inner atmosphere, as is present in this system. However, Hydra A shows multiple aligned cavities, suggesting that the last few major AGN outbursts are oriented in the same direction (Wise et al. 2007), allowing us to isolate undisturbed parts of its atmosphere. The deep data available permit an accurate measurement of its central $t_{\rm cool}/t_{\rm ff}$ profile. Furthermore, while Hydra A contains a second temperature component in its core, the cooler component contains only a small fraction of the mass (∼1/450 of the hot component, Hogan et al. 2017). Therefore, less uncertainty is expected to be introduced by single-temperature models than for clusters where the cooler

component is more noticeable (e.g., A496, ratio ∼50 rather than 450). Indeed, among the five clusters (including Hydra A) with deep *Chandra* data studied in Hogan et al. (2017) we found that the deprojected $(t_{\rm cool}/t_{\rm ff})_{\rm min}$ were consistent with being flat. Finally we note that the $t_{\rm cool}/t_{\rm ff}$ profile for the nearby cluster M87, which is resolvable to scales <1 kpc, also flattens to a floor over 10–15 bins, rather than to a sharp minimum (McNamara et al. 2016).

8. Conclusions

We have investigated cooling in cluster atmospheres using a sample of 57 clusters. These were selected as being the most suitable in which to simultaneously study hot atmospheres at low cluster-centric altitudes (<10 kpc) and to measure accurate total cluster masses to large radii. Our main findings are as follows.

1. $t_{\rm cool}/t_{\rm ff}$ provide no more predictive power for the onset of thermally unstable cooling than $t_{\rm cool}$ alone.
2. Using acceleration profiles that account for the central galaxy's mass, and cooling profiles that use both deprojected density and temperature, we find no cluster atmospheres with a $t_{\rm cool}/t_{\rm ff}$ minimum significantly below 10. Atmospheres with bright nebular emission and star formation lie in the range $10 < t_{\rm cool}/t_{\rm ff} < 35$, where the upper end of this range corresponds to the $t_{\rm cool}$ threshold for thermally unstable gas of 1 Gyr at 10 kpc.
3. The absence of clusters with $(t_{\rm cool}/t_{\rm ff})_{\rm min} < 10$ is inconsistent with models that assume thermally unstable cooling arises from linear density perturbations when $(t_{\rm cool}/t_{\rm ff})_{\rm min} < 10$. The observed range of $(t_{\rm cool}/t_{\rm ff})_{\rm min} \sim 10$–35 is consistent with models that assume pre-existing nonlinear perturbations, perhaps seeded by rising radio bubbles or gas sloshing.
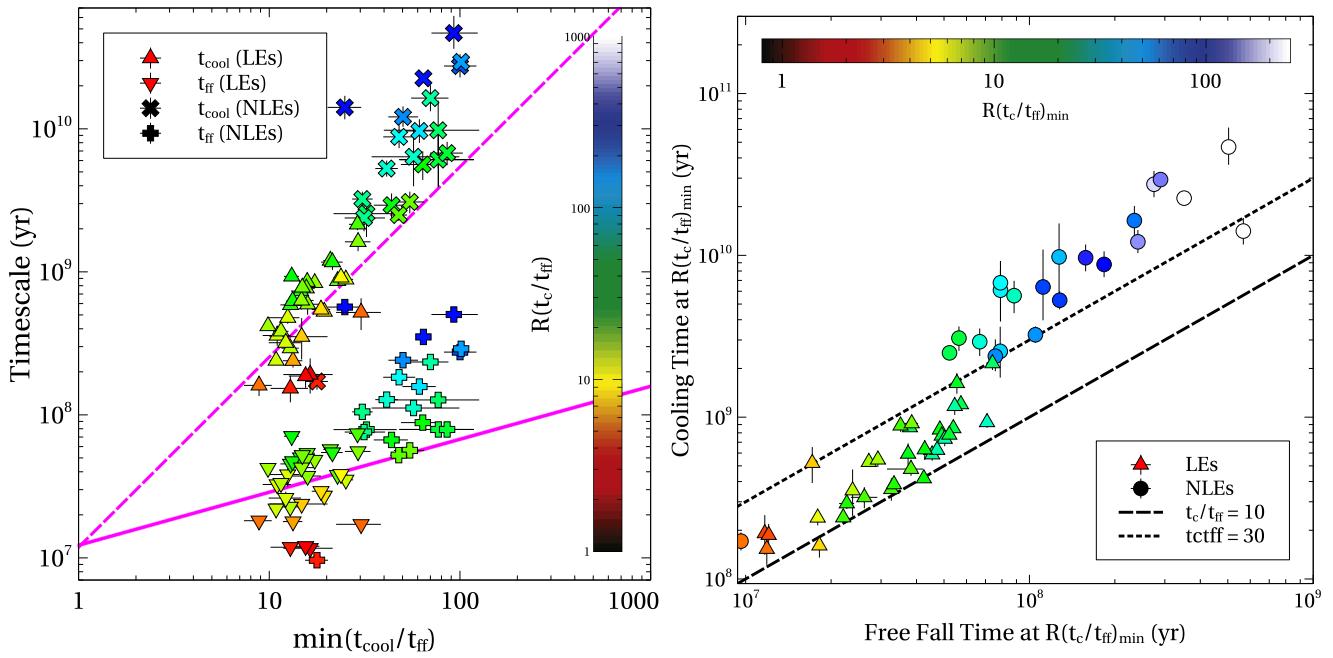
Figure 12. Left: numerator and denominator are plotted against the minimum cooling time to free-fall time ratio. NLE (proxy for non-cool cores) sources appear to show a trend in t_{ff} though this is almost certainly bias due to the large truncation radii of their profiles (see Section 6.2.1). Solid lines are fits to the LEs (cool cores only). We find a significant trend only for t_{cool}, showing that the numerator dominates the ratio. The color gradient shows correlated scatter in t_{ff} and t_{cool} that can be attributed to their co-dependence on density (see Section 6.2.1), which itself could explain the narrow range in observed $(t_{cool}/t_{ff})_{min}$. Right: strong correlation between t_{cool} and t_{ff} measured at the locations of the t_{cool}/t_{ff} minima; this again could naturally serve to narrow the range of observed $(t_{cool}/t_{ff})_{min}$, as highlighted by the color gradient with $R(t_{cool}/t_{ff})_{min}$.
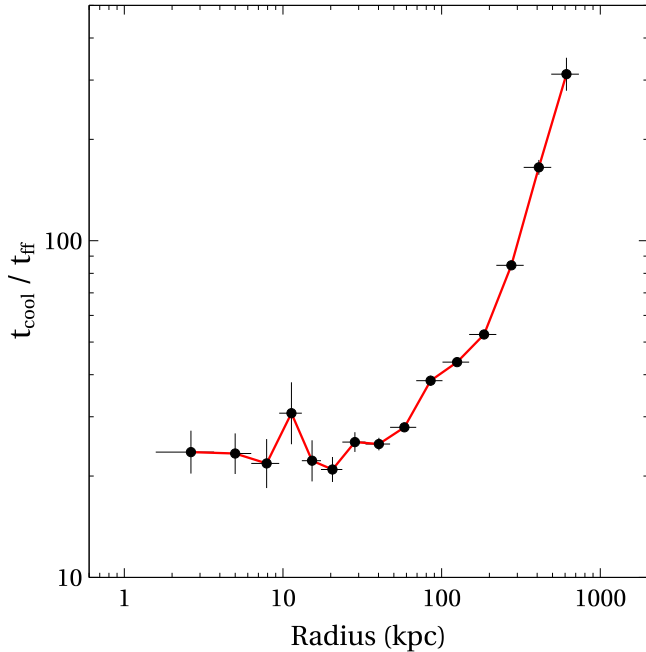
Figure 13. t_{cool}/t_{ff} profile for the Hydra A cluster. This system has the best resolved data near the location of the minimum in this profile. We do not see a rise to smaller radii, as seen in less well resolved systems. See the discussion in Section 7.

4. The small range of atmospheric gas densities and cooling times at low altitudes indicates AGN heating that is much gentler than predicted by many feedback models.

5. The small range in, and measured values of, $(t_{cool}/t_{ff})_{min}$ can be attributed to observational biases. Once the biases are accounted for, the spread in t_{cool}/t_{ff} at a fixed altitude is comparable to the spread in t_{cool} alone.

6. Cool-core entropy profiles are described by a broken power law: $K \propto r^{0.67}$ between $\sim$1–50 kpc and $K \propto r^{1.1}$ at larger radii. We find no evidence for flattening below $K \propto r^{0.67}$, or large ($\sim$5–20 kpc) isentropic cores.

7. A natural floor in t_{cool}/t_{ff} profiles arises from the measured shape of the inner entropy profile and an isothermal mass distribution. Among relaxed/non-merger systems we see no evidence for an upturn in t_{cool}/t_{ff} at small radius, and all systems are broadly consistent with a t_{cool}/t_{ff} floor.

Overall we find that local acceleration in the form of t_{ff} provides no additional information concerning gas condensation in galaxy clusters above the cooling time alone. The total cluster mass appears to play a role, and may set the baseline cooling level for the cluster. This will be investigated in an upcoming paper. Any weak trends with t_{ff} are likely secondary as this parameter effectively traces cluster mass, which may be the true underlying cause. Stimulated feedback via uplift appears to be a promising model for gas condensation but further work is required to test this.

Appendix A
Notes on Mass Profiles of Individual Clusters

Cluster mass profiles were calculated according to the prescription outlined in Section 4.2. Here we give additional notes on a subset of systems where either special attention was required or we found substantial differences from previously reported masses.

A2626: A relatively small cool-core cluster. Zhao et al. (2013) report an $M_{500} = (1.81 \pm 0.14) \times 10^{14} M_\odot$ at $R_{500} = 850$ kpc, which is 25% higher than our mass at an equivalent radius, though we note that extrapolation of our profiles beyond R_{2500} is uncertain.

A3667: This is a non-cool-core cluster that is tagged as a merger in Vikhlinin et al. (2009), who found $M_{500} = (6.74 \pm 0.09) \times 10^{14} M_\odot$. The total cluster mass reported could be underestimated as a result of this system being substantially out of hydrostatic equilibrium.

A2142: A seemingly relaxed non-cool-core cluster that contains a distinct cold front (Owers et al. 2011). Nevertheless, our calculated mass is in reasonable agreement with the $M_{500} = (11.70 \pm 0.45) \times 10^{14} M_\odot$ reported by Vikhlinin et al. (2009).

A3376: This non-cool-core cluster does not have a clear central BCG and was previously found to not be described well by either an NFW or King model (Ettori et al. 2002). A convergent fit is found when the isothermal component is minimized (consistent with negligible central stellar component) though the large NFW scale radius means that the fit is essentially reverting to a power law, suggesting that this object is perhaps a small group. The data is insufficient to recover central atmospheric properties inwards of ∼15 kpc and so the uncertain inner mass profile is not considered overly concerning. Our reported M_{2500} is in reasonable agreement with the ACCEPT mass profile for this object (Cavagnolo et al. 2009).

A1644: This system is a complex merging cool-core (Reiprich et al. 2004), containing a major substructure approximately 700 kpc north–east of the main cluster that itself contains a spiral surface brightness feature indicative of ongoing sloshing. The BCG is a very large cD extending ∼80 kpc. Our modeling is limited to an outermost radius of 424 kpc, beyond which contamination from the substructure causes unstable fits, though a β component is still not favored. Our recovered M_{2500} appears low compared to the total cluster masses (M_{500}) of (4.0–4.5) $\times 10^{14} M_\odot$ reported by Vikhlinin et al. (2009) (X-ray) and Girardi et al. (1998) (optical), although it is in reasonable agreement with the mass at same radius reported in ACCEPT (Cavagnolo et al. 2009). Note that while our mass estimate is for the main cluster structure only and therefore likely to underestimate the total mass if extrapolated beyond R_{2500}, the mass is relevant for the dynamical times required within our region of interest. This is particularly true at low altitudes where the large BCG dominates the potential.

A2319: A hot and rather massive non-cool-core cluster. Extrapolation of the profile is in agreement with the M_{500} and M_{200} masses found by Reiprich & Böhringer (2002).

A1413: We recover a higher M_{2500} than Allen et al. (2008) ($M_{2500} \sim 3.5 \times 10^{14} M_\odot$ at 599 kpc) and Vikhlinin et al.

(2006) (∼3.0 $\times 10^{14} M_\odot$). The BCG of this cluster appears to be undergoing a merger and hence its inferred isothermal velocity dispersion may be biased high. To test for this we re-fit but with the fixed isothermal component halved, and find that the NFW component compensates to return an almost identical M_{2500}.

A2034: This is a large diffuse cluster without an obvious central BCG. The best-fit NFW is recovered when minimizing the isothermal component, consistent with the lack of a central stellar potential.

PKS 0745–191: Cool-core cluster with clear cavity system. Main et al. (2017) and Allen et al. (2008) report marginal disagreement in mass, reporting $M_{2500} = 3.3 \times 10^{14} M_\odot$ and $M_{2500} = 4.8 \times 10^{14} M_\odot$ at $R_{2500} = 600, 680$ kpc respectively. Our recovered cluster mass lies between these values.

Hercules A: The BCG of this cluster contains the powerful FR-I radio source 3C348. Our M_{2500} is approximately half that reported by Main et al. (2017) (∼2.1 $\times 10^{14} M_\odot$ at $R_{2500} \approx 500$ kpc) although it is in good agreement with the $M_{2500} = 1.23 \times 10^{14} M_\odot$ at 423 kpc reported by Comis et al. (2011).

A2204: A well studied and massive cool-core cluster. Two M_{2500} values could be found in the literature, with 4.1 $\times 10^{14} M_\odot$ and 5.5 $\times 10^{14} M_\odot$ reported by Allen et al. (2008) and Main et al. (2017) at $R_{2500} \approx 630$ and 700 kpc respectively. Further, Vikhlinin et al. (2009) reported $M_{500} \approx 8.9 \times 10^{14} M_\odot$. The inferred velocity dispersion appears high, and is perhaps biased by ongoing star formation in the BCG Oonk et al. (2011). Our M_{2500} is in agreement with the Allen et al. (2008) number, lying between this and the Main et al. (2017) value.
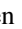
A1991: Small cool-core cluster with a relatively large BCG. Vikhlinin et al. (2006) reported $M_{2500} \approx 0.63 \times 10^{14} M_\odot$ and $M_{500} \approx 1.23 \times 10^{14} M_\odot$, with Comis et al. (2011) finding $M_{2500} \approx 0.32 \times 10^{14} M_\odot$ at $R_{2500} = 279$ kpc. Our outermost annulus extends to 779.1 kpc although there appears to be emission beyond this, and indeed the inclusion of a β parameter significantly improves the fit. This increases our M_{2500} from ∼0.43 to ∼0.55 $\times 10^{14} M_\odot$, in agreement with the Vikhlinin et al. (2006) value.

Zw7160: This cluster is also known by the names MS 1455.0 +2232 and ZwCl 1454.8+2233. Comis et al. (2011) find an $M_{2500} \approx 1.53 \times 10^{14} M_\odot$ at 436 kpc. Martino et al. (2014) used both *XMM-Newton* and *Chandra* data to independently calculate two estimates of M_{2500} for this cluster, finding $M_{2500} \approx 1.58 \times 10^{14} M_\odot$ and $M_{2500} \approx 1.89 \times 10^{14} M_\odot$ respectively. The relatively high redshift of this cluster means its atmosphere can be traced to a radial distance of almost 3 Mpc. Modeling out to $R \approx 2742$ kpc gives an M_{2500} in approximate agreement with the previously reported values. However, our fits are poor since there is no discernible cluster signal beyond ∼1.2 Mpc. Restricting ourselves to $R \lesssim 1.2$ Mpc we recover a statistically improved fit, though our mass is now slightly above previously found values. We note that our restricted radial range is reasonably close to that used by Martino et al. (2014).

A1758: This is a complex, distorted, and diffuse non-cool-core cluster with no obvious center or BCG. Further complicating the system is a secondary cluster about 2 Mpc to the south. If we truncate our fitted region to ≲875 kpc so as to exclude the secondary object, include a β parameter to allow for excluded emission, and minimize the isothermal component

in recognition of the lack of a clear stellar component at the cluster center, then we recover a convergent fit. Our M_{2500} is higher than that found by Comis et al. (2011) ($M_{2500} = 0.052 \times 10^{14}\, M_\odot$ at 144 kpc).

ORCID iDs

B. R. McNamara ⬤ https://orcid.org/0000-0002-2622-2627
F. A. Pulido ⬤ https://orcid.org/0000-0003-3595-937X
P. E. J. Nulsen ⬤ https://orcid.org/0000-0003-0297-4493
A. N. Vantyghem ⬤ https://orcid.org/0000-0003-4227-4838
A. C. Edge ⬤ https://orcid.org/0000-0002-3398-6916
Iu. Babyk ⬤ https://orcid.org/0000-0003-3165-9804
M. McDonald ⬤ https://orcid.org/0000-0001-5226-8349

References

Allen, S. W., Rapetti, D. A., Schmidt, R. W., et al. 2008, MNRAS, 383, 879
Anders, E., & Grevesse, N. 1989, GeCoA, 53, 197
Arnaud, K. A. 1996, in ASP Conf. Ser. 101, Astronomical Data Analysis Software and Systems V, ed. G. H. Jacoby & J. Barnes (San Francisco, CA: ASP), 17
Baldry, I. K., Glazebrook, K., & Driver, S. P. 2008, MNRAS, 388, 945
Balucinska-Church, M., & McCammon, D. 1992, ApJ, 400, 699
Bell, E. F., McIntosh, D. H., Katz, N., & Weinberg, M. D. 2003, ApJS, 149, 289
Bîrzan, L., Rafferty, D. A., McNamara, B. R., Wise, M. W., & Nulsen, P. E. J. 2004, ApJ, 607, 800
Borgani, S., Dolag, K., Murante, G., et al. 2006, MNRAS, 367, 1641
Brighenti, F., Mathews, W. G., & Temi, P. 2015, ApJ, 802, 118
Cavagnolo, K. W., Donahue, M., Voit, G. M., & Sun, M. 2008, ApJL, 683, L107
Cavagnolo, K. W., Donahue, M., Voit, G. M., & Sun, M. 2009, ApJS, 182, 12
Choudhury, P. P., & Sharma, P. 2016, MNRAS, 457, 2554
Clowe, D., Bradač, M., Gonzalez, A. H., et al. 2006, ApJL, 648, L109
Comis, B., de Petris, M., Conte, A., Lamagna, L., & de Gregori, S. 2011, MNRAS, 418, 1089
Cowie, L. L., Fabian, A. C., & Nulsen, P. E. J. 1980, MNRAS, 191, 399
Crawford, C. S., Allen, S. W., Ebeling, H., Edge, A. C., & Fabian, A. C. 1999, MNRAS, 306, 857
David, L. P., Jones, C., & Forman, W. 1996, ApJ, 473, 692
David, L. P., Nulsen, P. E. J., McNamara, B. R., et al. 2001, ApJ, 557, 546
Donahue, M., Horner, D. J., Cavagnolo, K. W., & Voit, G. M. 2006, ApJ, 643, 730
Donahue, M., Voit, G. M., O'Dea, C. P., Baum, S. A., & Sparks, W. B. 2005, ApJL, 630, L13
Edge, A. C. 2001, MNRAS, 328, 762
Ettori, S., De Grandi, S., & Molendi, S. 2002, A&A, 391, 841
Fabian, A. C. 1994, ARA&A, 32, 277
Fabian, A. C. 2012, ARA&A, 50, 455
Fabian, A. C., Reynolds, C. S., Taylor, G. B., & Dunn, R. J. H. 2005, MNRAS, 363, 891
Fisher, D., Illingworth, G., & Franx, M. 1995, ApJ, 438, 539
Freeman, P. E., Kashyap, V., Rosner, R., & Lamb, D. Q. 2002, ApJS, 138, 185
Fruscione, A., McDowell, J. C., Allen, G. E., et al. 2006, Proc. SPIE, 6270, 62701V
Gaspari, M., Ruszkowski, M., & Oh, S. P. 2013, MNRAS, 432, 3401
Gaspari, M., Ruszkowski, M., & Sharma, P. 2012, ApJ, 746, 94
Gaspari, M., Temi, P., & Brighenti, F. 2017, MNRAS, 466, 677
Girardi, M., Giuricin, G., Mardirossian, F., Mezzetti, M., & Boschin, W. 1998, ApJ, 505, 74
Gutierrez, K., & Krawczynski, H. 2005, ApJ, 619, 161
Heckman, T. M., Baum, S. A., van Breugel, W. J. M., & McCarthy, P. 1989, ApJ, 338, 48
Henry, J. P., & Briel, U. G. 1995, ApJL, 443, L9
Hillel, S., & Soker, N. 2016, MNRAS, 455, 2139
Hillel, S., & Soker, N. 2017, MNRAS, 466, 39
Hlavacek-Larrondo, J., Fabian, A. C., Edge, A. C., et al. 2012, MNRAS, 421, 1360
Hlavacek-Larrondo, J., McDonald, M., Benson, B. A., et al. 2015, ApJ, 805, 35
Hogan, M. T., Edge, A. C., Geach, J. E., et al. 2015a, MNRAS, 453, 1223
Hogan, M. T., Edge, A. C., Hlavacek-Larrondo, J., et al. 2015b, MNRAS, 453, 1201

Hogan, M. T., McNamara, B. R., Pulido, F., et al. 2017, ApJ, 837, 51
Johnstone, R. M., Fabian, A. C., & Nulsen, P. E. J. 1987, MNRAS, 224, 75
Joye, W. A., & Mandel, E. 2003, in ASP Conf. Ser. 295, Astronomical Data Analysis Software and Systems XII, ed. H. E. Payne, R. I. Jedrzejewski, & R. N. Hook (San Francisco, CA: ASP), 489
Kalberla, P. M. W., Burton, W. B., Hartmann, D., et al. 2005, A&A, 440, 775
Koopmans, L. V. E., Bolton, A., Treu, T., et al. 2009, ApJL, 703, L51
Lakhchaura, K., Deep Saini, T., & Sharma, P. 2016, arXiv:1601.02347
Li, Y., & Bryan, G. L. 2014, ApJ, 789, 153
Li, Y., Bryan, G. L., Ruszkowski, M., et al. 2015, ApJ, 811, 73
Liedahl, D. A., Osterheld, A. L., & Goldstein, W. H. 1995, ApJL, 438, L115
Ma, C.-J., McNamara, B. R., Nulsen, P. E. J., Schaffer, R., & Vikhlinin, A. 2011, ApJ, 740, 51
Macario, G., Markevitch, M., Giacintucci, S., et al. 2011, ApJ, 728, 82
Main, R. A., McNamara, B. R., Nulsen, P. E. J., Russell, H. R., & Vantyghem, A. N. 2017, MNRAS, 464, 4360
Markevitch, M., Gonzalez, A. H., David, L., et al. 2002, ApJL, 567, L27
Markevitch, M., Govoni, F., Brunetti, G., & Jerius, D. 2005, ApJ, 627, 733
Martino, R., Mazzotta, P., Bourdin, H., et al. 2014, MNRAS, 443, 2342
McCourt, M., Sharma, P., Quataert, E., & Parrish, I. J. 2012, MNRAS, 419, 3319
McDonald, M., Benson, B. A., Vikhlinin, A., et al. 2013, ApJ, 774, 23
McDonald, M., McNamara, B. R., van Weeren, R. J., et al. 2015, ApJ, 811, 111
McDonald, M., Veilleux, S., Rupke, D. S. N., & Mushotzky, R. 2010, ApJ, 721, 1262
McNamara, B. R., & Nulsen, P. E. J. 2007, ARA&A, 45, 117
McNamara, B. R., & Nulsen, P. E. J. 2012, NJPh, 14, 055023
McNamara, B. R., Russell, H. R., Nulsen, P. E. J., et al. 2014, ApJ, 785, 44
McNamara, B. R., Russell, H. R., Nulsen, P. E. J., et al. 2016, arXiv:1604.04629
Meece, G. R., O'Shea, B. W., & Voit, G. M. 2015, ApJ, 808, 43
Mewe, R., Gronenschild, E. H. B. M., & van den Oord, G. H. J. 1985, A&AS, 62, 197
Nagai, D., Kravtsov, A. V., & Vikhlinin, A. 2007, ApJ, 668, 1
Nulsen, P. E. J. 1986, MNRAS, 221, 377
Nulsen, P. E. J., & McNamara, B. R. 2013, AN, 334, 386
Nulsen, P. E. J., Powell, S. L., & Vikhlinin, A. 2010, ApJ, 722, 55
O'Dea, C. P., Baum, S. A., Privon, G., et al. 2008, ApJ, 681, 1035
Oonk, J. B. R., Hatch, N. A., Jaffe, W., Bremer, M. N., & van Weeren, R. J. 2011, MNRAS, 414, 2309
Owers, M. S., Nulsen, P. E. J., & Couch, W. J. 2011, ApJ, 741, 122
Panagoulia, E. K., Fabian, A. C., & Sanders, J. S. 2014, MNRAS, 438, 2341
Peterson, J. R., Kahn, S. M., Paerels, F. B. S., et al. 2003, ApJ, 590, 207
Pizzella, A., Corsini, E. M., Dalla Bontà, E., et al. 2005, ApJ, 631, 785
Pizzolato, F., & Soker, N. 2005, ApJ, 632, 821
Pizzolato, F., & Soker, N. 2010, MNRAS, 408, 961
Poggianti, B. M. 1997, A&AS, 122, 399
Ponman, T. J., Cannon, D. B., & Navarro, J. F. 1999, Natur, 397, 135
Ponman, T. J., Sanderson, A. J. R., & Finoguenov, A. 2003, MNRAS, 343, 331
Prasad, D., Sharma, P., & Babul, A. 2015, ApJ, 811, 108
Rafferty, D. A., McNamara, B. R., & Nulsen, P. E. J. 2008, ApJ, 687, 899
Rafferty, D. A., McNamara, B. R., Nulsen, P. E. J., & Wise, M. W. 2006, ApJ, 652, 216
Randall, S. W., Forman, W. R., Giacintucci, S., et al. 2011, ApJ, 726, 86
Rawle, T. D., Edge, A. C., Egami, E., et al. 2012, ApJ, 747, 29
Reiprich, T. H., & Böhringer, H. 2002, ApJ, 567, 716
Reiprich, T. H., Sarazin, C. L., Kempner, J. C., & Tittley, E. 2004, ApJ, 608, 179
Revaz, Y., Combes, F., & Salomé, P. 2008, A&A, 477, L33
Romanowsky, A. J., & Kochanek, C. S. 2001, ApJ, 553, 722
Russell, H. R., Fabian, A. C., McNamara, B. R., & Broderick, A. E. 2015, MNRAS, 451, 588
Russell, H. R., McDonald, M., McNamara, B. R., et al. 2017, ApJ, 836, 130
Russell, H. R., McNamara, B. R., Edge, A. C., et al. 2014, ApJ, 784, 78
Russell, H. R., McNamara, B. R., Fabian, A. C., et al. 2016, MNRAS, arXiv:1602.05962
Russell, H. R., Sanders, J. S., & Fabian, A. C. 2008, MNRAS, 390, 1207
Russell, H. R., Sanders, J. S., Fabian, A. C., et al. 2010, MNRAS, 406, 1721
Salomé, P., & Combes, F. 2003, A&A, 412, 657
Samuele, R., McNamara, B. R., Vikhlinin, A., & Mullis, C. R. 2011, ApJ, 731, 31
Sanders, J. S., & Fabian, A. C. 2007, MNRAS, 381, 1381
Sanders, J. S., & Fabian, A. C. 2008, MNRAS, 390, L93
Sanders, J. S., & Fabian, A. C. 2011, MNRAS, 412, L35
Sanderson, A. J. R., Edge, A. C., & Smith, G. P. 2009, MNRAS, 398, 1698

Santos, J. S., Tozzi, P., Rosati, P., & Böhringer, H. 2010, A&A, 521, A64
Schlegel, D. J., Finkbeiner, D. P., & Davis, M. 1998, ApJ, 500, 525
Sharma, P., McCourt, M., Quataert, E., & Parrish, I. J. 2012, MNRAS, 420, 3174
Sijacki, D., & Springel, V. 2006, MNRAS, 366, 397
Skrutskie, M. F., Cutri, R. M., Stiening, R., et al. 2006, AJ, 131, 1163
Soker, N. 2016, NewAR, 75, 1
Tozzi, P., & Norman, C. 2001, ApJ, 546, 63
Tremblay, G. R., O'Dea, C. P., Baum, S. A., et al. 2015, MNRAS, 451, 3768
Tremblay, G. R., Oonk, J. B. R., Combes, F., et al. 2016, Natur, 534, 218
Vantyghem, A. N., McNamara, B. R., Russell, H. R., et al. 2016, ApJ, 832, 148
Vikhlinin, A., Burenin, R. A., Ebeling, H., et al. 2009, ApJ, 692, 1033
Vikhlinin, A., Kravtsov, A., Forman, W., et al. 2006, ApJ, 640, 691

Voit, G. M., & Donahue, M. 2005, ApJ, 634, 955
Voit, G. M., & Donahue, M. 2015, ApJL, 799, L1
Voit, G. M., Donahue, M., Bryan, G. L., & McDonald, M. 2015, Natur, 519, 203
Voit, G. M., Kay, S. T., & Bryan, G. L. 2005, MNRAS, 364, 909
Voit, G. M., Meece, G., Li, Y., et al. 2017, ApJ, 845, 80
Wang, Y., Xu, H., Gu, L., et al. 2010, MNRAS, 403, 1909
White, J. A., Canning, R. E. A., King, L. J., et al. 2015, MNRAS, 453, 2718
Wise, M. W., McNamara, B. R., Nulsen, P. E. J., Houck, J. C., & David, L. P. 2007, ApJ, 659, 1153
Yang, H.-Y. K., & Reynolds, C. S. 2016, ApJ, 818, 181
Zhao, H.-H., Jia, S.-M., Chen, Y., et al. 2013, ApJ, 778, 124
Zhuravleva, I., Churazov, E., Schekochihin, A. A., et al. 2014, Natur, 515, 85